Arabian Journal of Chemistry (2022) **15**, 103851

King Saud University

Arabian Journal of Chemistry

www.ksu.edu.sa
www.sciencedirect.com

ORIGINAL ARTICLE

Greener pastures in evaluating antidiabetic drug for a quinoxaline Derivative: Synthesis, Characterization, Molecular Docking, *in vitro* and HSA/DFT/XRD studies

Mohcine Missioui [a], Salma Mortada [b], Walid Guerrab [a], Güneş Demirtaş [c], Joel T. Mague [d], M'hammed Ansar [a], My El Abbes Faouzi [b], E.M. Essassi [e], Yassin T.H. Mehdar [f], Faizah S. Aljohani [f], Musa A. Said [f], Youssef Ramli [a,*]

[a] *Laboratory of Medicinal Chemistry, Drug Sciences Research Center, Faculty of Medicine and Pharmacy, Mohammed V University in Rabat, Morocco*
[b] *Laboratories of Pharmacology and Toxicology, Faculty of Medicine and Pharmacy, Mohammed V University in Rabat, Morocco*
[c] *Ondokuz Mayıs University, Faculty of Arts and Sciences, Department of Physics, 55139 Samsun, Turkey*
[d] *Department of Chemistry, Tulane University, New Orleans, LA 70118, USA*
[e] *Laboratory of Heterocyclic Organic Chemistry, Faculty of Sciences, Mohammed V University, Rabat, Morocco*
[f] *Department of Chemistry, Taibah University, Madinah, King Saudi Arabia*

Received 6 January 2022; accepted 22 March 2022

KEYWORDS

Quinoxaline;
1,2,3-triazole;
XRD;
Hirshfeld Surface Analysis (HSA), DFT;
Anti-diabetic activity;
Molecular docking

Abstract In an effort to develop a potent antidiabetic drug, new quinoxaline derivative, 2-(4-((3-methyl-2-oxoquinoxalin-1(2H)-yl)methyl)-4,5-dihydro-1H-1,2,3-triazol-1-yl)-N-(p-tolyl)acetamide (MOQTA) was synthesized and characterized by XRD and various spectroscopic tools (IR, ^{1}H &^{13}C NMR, ESI-MS). The geometric optimization of the molecule was calculated with Density Functional Theory (DFT) method by B3LYP with a 6–311 + + G(d,p) basis set. Frontier Molecular Orbitals (FMOs) and Molecular Electrostatic Potential (MEP) surfaces of the title compound were generated. Furthermore, Hirshfeld surface analysis (HSA) and 2D fingerprint plots were presented. The calculated MEP and HSA surface interactions were compared in terms of hydrogen bonds and π-π stacking interactions obtained by X-ray packing analyses. X-ray crystallographic structure analysis revealed that the N—HN, C—HO and C—HN intermolecular hydrogen bonds were in agreement with those obtained by HSA. Moreover, MOQTA was assessed for its *in vitro*

* Corresponding author.
E-mail address: y.ramli@um5s.net.ma (Y. Ramli).
Peer review under responsibility of King Saud University.

Production and hosting by Elsevier

https://doi.org/10.1016/j.arabjc.2022.103851

anti-diabetic activity. Likewise, molecular docking analyses were conducted to examine the binding mode between MOQTA and the enzymes α-glucosidase and α-amylase. Finally, the physicochemical, pharmacokinetic and toxicological properties of MOQTA have been evaluated by using *in silico* absorption, distribution, metabolism, excretion and toxicity analysis prediction.

1. Introduction

Small heterocycles ring's therapeutic and industrial importance, having nitrogen atoms, has attracted much attention. Examples of heterocycles studied as candidates in drug discovery are: triazoles, quinoxalines and acetamides. They have an important role in medicinal chemistry. Quinoxaline and its derivatives have attracted significant considerations due to their pharmacological activities (Ramli and Essassi, 2015; Ramli et al., 2014; Abad et al., 2020) and industrial properties (Allali et al., 2019; Lgaz, 2015; Laabaissi et al., 2020). This heterocycle already preset in variety of biological active substance and present anti-microbial (Badran et al., 2003; Singh et al., 2010), anti-fungal (Wagle et al., 2008), anti-malarial (Hui et al., 2006), anti-bacterial (Griffith et al., 1992; El-Sabbagh et al., 2009), anti-HIV (Loriga et al., 1997; Balzarini et al., 2000), anti-tuberculosis (Carta et al., 2006), anti-protozoal (Ancizu et al., 2010), anti-inflammatory (Carta et al., 2001), anthelmintic (Guillon et al., 2004) and anti-cancer (Gupta et al., 2005) properties. In addition, quinoxaline derivatives possess anticorrosion characteristics (Lgaz et al., 2016; Zarrok et al., 2012; El Ouali et al., 2010; Abboud et al., 2007; Zarrok et al., 2012; Tazouti et al., 2016; el Aoufir et al., 2016). Similarly, the triazole ring system is linked to biological and pharmacological activities as anti-inflammatory (Abdel-Megeed et al., 2009), antifungal (Nowaczyk and Modzelewska-Banachiewicz, 2008), antibacterial (Foroumadi et al., 2003), antihypertensive (Sato et al., 2009), anti-Alzheimer's disease (Missioui et al., 2022), anti-COVID-19 (Missioui et al., 2022; Zhang et al., 2020) and anticancer (Shivarama Holla et al., 2003) activity. Also, this heterocyclic scaffold can tolerate reductive/oxidative and basic/acid hydrolysis environments, displaying high-level aromatic endurance to metabolic degradation (Tron et al., 2008; Ferreira et al., 2010; Lauria et al., 2014). Diabetes affects around a quarter of the World's population, and this figure is expected to increase to 700 million by 2045 (Nazir et al., 2018). The identified α-amylase and α-glucosidase inhibitors, as miglitol, voglibose, and acarbose, have been tried to treat type 2 diabetes(T2DM). Nevertheless, it was interesting to discover the novel α-amylase and α-glucosidase inhibitors because of the undesirable effects (for example, diarrhea and stomachache) of the existing α-amylase and α-glucosidase inhibitors. Therefore, the therapeutic use of inhibitors of α-amylase and α-glucosidase in the medication of T2DM side-effect has been considered (Gu et al., 2020; Alomari et al., 2021; Hussain et al., 2021; Tavaf et al., 2020). A variety of molecules, including quinoxaline (Ramli and Essassi, 2015; Missioui et al., 2021) *N*-arylacetamides (Missioui et al., 2021; Wang et al., 2017; Moghimi et al., 2020; Asath et al., 2016) triazole (Ye et al., 2019) have been reported as potential antidiabetic agents. Because of this application and as part of our ongoing work (Zaoui et al., 2021; Abad et al., 2021; Abad et al., 2021; Guerrab et al., 2021; Guerrab et al., 2019; , xxxx), more recent work has reported synthesizing a novel *N*-arylacetamides quinoxaline-based compound as an anti-diabetic drug (Missioui et al., 2021). Continuing our ongoing research to discover novel quinoxaline-based compounds and improve this antidiabetic activity, the title quinoxaline compound including triazole was synthesized, charecterized by crystallographic techniques., and assessed as an antidiabetic agent. Molecular docking, geometric optimization, MEP surfaces, FMOs, and HSA were calculated for the title compound. These studies highlighted the interaction of the title compound as a promising α-amylase and α-glucosidase inhibitor.

2. Experimental section

2.1. Synthesis and crystallization

All chemicals, including solvents, were obtained from commercial sources of high purity and used as received. Follow-up of the reactions were made by TLC. In a Büchi Melting Point SMP-20 apparatus, the compound's melting point was determined and uncorrected. ^{1}H NMR and ^{13}C NMR spectra were collected using a Bruker Avance 300 NMR Spectrometer in DMSO d_6 and a « JNM-ECZ500R/S1 FT NMR System de JEOL » spectrometer, using TMS as the internal standard and CHLOROFORM-D as solvent. FT-IR spectra were collected using the Bruker-VERTEX 70 device. Mass spectra were recorded on an API 3200 LC/MS/MS mass spectrometer using electrospray ionization (ESI).

2.1.1. 3-Methyl-1H-quinoxalin-2-one (MQO)

Compound MQO was synthesized following a procedure similar to that of Hinsberg (Hinsberg, 1887); using *O*-phenylenediamine (15 mmol) and ethyl pyruvate (22.5 mmol) in HCl 4.4 N at room temperature for 30 min (Scheme 1).

2.1.2. 3-methyl-1-(prop-2-yn-1-yl)quinoxalin-2(1H)-one (MPQ)

To 15 mL of DMF and MQO (0.5 g, 3.11 mmol) was added potassium carbonate (0.5 g, 3.73 mmol), propargyl bromide (0.41 mL, 3.11 mmol), and tetra-nbutylammonium bromide. The solution was stirred at 25 ^{0}C for 24 h. After filtration, all volatiles were removed under low pressure. The recrystallization is carried out in ethanol to afford MPQ as colorless crystals in a good (68%) yield. (Benzeid et al., 2009) (Scheme 1).

2.1.3. 2-azido-N-(p-tolyl)acetamide (ATA)

A previous procedure (Missioui et al., 2022) was used to afford 2-chloro-N-(p-tolyl)acetamide, precursor. 2-chloro-N-(p-tolyl) acetamide (0.011 mol) and sodium azide (0.015 mol) were dissolved in a mixture of ethanol/water (2:1 ratio) then refluxed for 24 h at 80 °C. After completing the reaction, the compound ATA: 2-azido-N-(p-tolyl)acetamide precipitated, filtered, washed with cold water, and recrystallized from ethanol.

2.1.4. 2-(4-((3-methyl-2-oxoquinoxalin-1(2H)-yl)methyl)-1H-1,2,3-triazol-1-yl)-N-(p-tolyl) acetamide (MOQTA)

To a solution of MPQ (0.5 mmol), in a water–ethanol mixture (5/15 mL), 2-azido-*N*-phenyl)acetamide (0.65 mmol) was added with sodium ascorbate and a catalytic amount of copper sulphate. After stirring, under reflux for 24 h, the solution was concentrated. The residue was washed with water and purified by column chromatography on silica gel using a hexane/ethyl

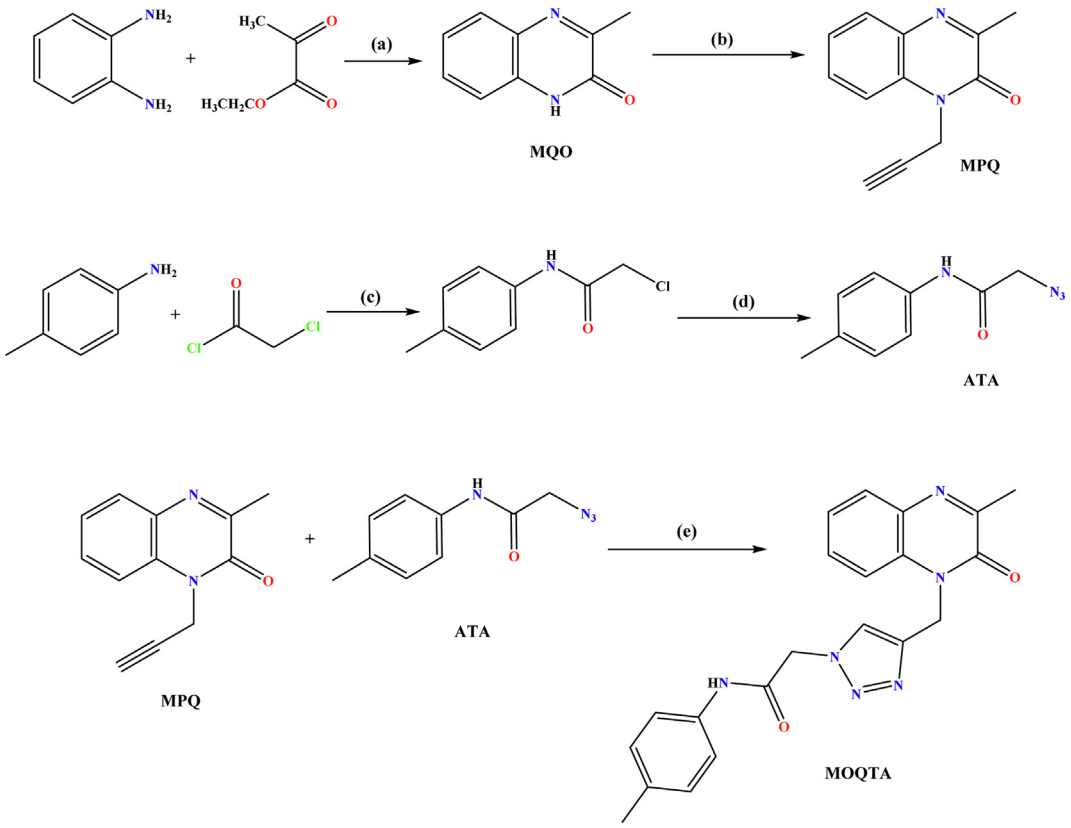

Scheme 1 Synthesis pathway of 2-(4-((3-methyl-2-oxoquinoxalin-1(2H)-yl)methyl)-1H-1,2,3-triazol-1-yl)-*N*-(p-tolyl) acetamide (MOQTA). Reagents and conditions: (a) HCl 4 N,rt; (b) K_2CO_3, propargyl bromide, TBAB, DMF, rt, 24 h; (c) THF, 0 °C; (d); NaN_3, DMF, 40 °C; (e) $CuSO_4$, Sodium ascorbate, EtOH / H_2O.

acetate (9/1) mixture as eluent. The solid product isolated was recrystallized from ethanol to afford a light yellow block-like specimen of compound MOQTA. (Scheme 1).

2.2. X-Ray crystal data collection

A light-yellow block-like sample of MOQTA of dimensions 0.197 mm × 0.250 mm × 0.268 mm, was mounted on a polymer loop in a cold nitrogen stream on a Bruker Smart APEX CCD diffractometer equipped with a fine-focus sealed tube (Mo-Kα, λ = 0.71073 Å) and a graphite monochromator. The complete sphere of data was processed using SAINT (Bruker APEX3, SAINT, SADABS SHELXTL, Bruker AXS, Inc., Madison, WI., 2016). The structure was solved by direct methods and refined by the full-matrix least-squares method on F2 using SHELXT and SHELXL programs (Sheldrick, 2015; Sheldrick, 2015). The molecular and packing diagrams were generated using DIAMOND (Brandenburg and Putz, 2012). A group of 1565 reflections having $I/\sigma(I) \geq 13$ was analyzed with *CELL_NOW* (Sheldrick, 2008) which showed the crystal to be twinned by a 180° rotation about the *a*-axis. The data were integrated with *SAINT* (Bruker-AXS and Madison, 2019) using the two-component orientation matrix generated by *CELL_NOW*. The structure is in (Fig. 1), and crystal and refinement (refined as a 2-component twin) details are presented in Table 1.

The structure was solved and refined using the Bruker SHELXTL Software Package, using the space group P 1 21/n 1, with Z = 4 for the formula unit, $C_{21}H_{20}N_6O_2$. The final anisotropic full-matrix least-squares refinement on F^2 with 265 variables converged at R1 = 5.27%, for the observed data and wR2 = 14.53% for all data. The goodness-of-fit was 1.067. The largest peak in the final difference electron density synthesis was 0.344 e-/Å3, and the largest hole was −0.230 e-/Å^3 with an RMS deviation of 0.053 e-/Å^3. Based on the final model, the calculated density was 1.400 g/cm^3 and F(000), 816 e-.

The supplementary crystallographic data for this paper are available: **CCDC 2073886**.

2.3. Biological activity

All chemicals and solvents were purchased from Sigma–Aldrich and used as received.

2.3.1. Enzyme inhibitory activities

1) α-Glucosidase inhibition assay.

The α-glucosidase inhibitory activity was performed using ρ-nitrophenyl-α-D-glucopyranoside as a substrate (Kee et al., 2013; Mortada et al., 2022) with minor modifications. Also,

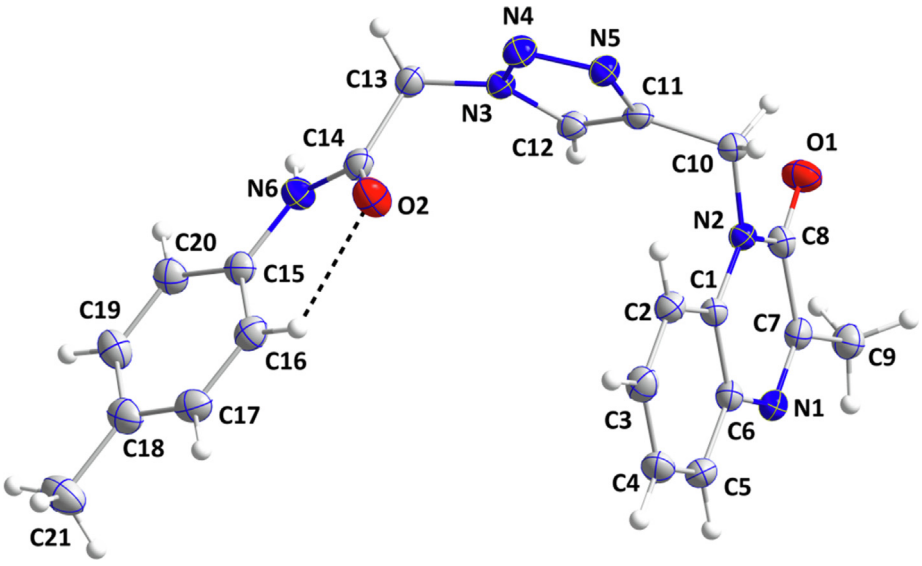

Fig. 1 The MOQTA molecule with labeling scheme and 50% probability ellipsoids.

the detailed protocol was described in our previous work (Hashim et al., 2013).

2.3.2. *Antioxidant activity*

For the protocol used to evaluate the antioxidant activity, see the reported method by Mortada et al. (Hashim et al., 2013), Tuberoso et al. (Tuberoso et al., 2013).

2.4. *Computational procedure*

Geometrical optimization of the title compound was calculated using Gaussian 03 program package (Frisch et al., 2004). This operation used the density functional theory by Becke's three-parameter hybrid functional (Becke, 1993) with Lee–Yang–Parr correlation functional (Lee et al., 1988; Miehlich et al., 1989) (B3LYP) approach in conjunction with the 6–311 + + G(d,p) basis set (Pople et al., 1986). The data obtained by XRD was used as initial values. FMO, MEP map and harmonic vibrational bands were generated using GaussView molecular visualization program (Frisch et al., 2007).

HSA (Spackman and Byrom, 1997; McKinnon et al., 1998) of the mole AutoDock Vina program in the crystal structure and 2D fingerprint (Spackman and McKinnon, 2002) plots were formed using Crystal Explorer 3.0 computer program (Wolff et al., 2012) using the CIF file.

2.5. *Docking methodology*

The docking study was carried out against α -glucosidase and α -amylase enzymes. The crystal structure of α-amylase (PDB Id: 4GQR; resolution 1.2 Å) (Williams, 2012) and α-glucosidase (PDB Id: 5NN5; resolution 2.0 Å) (xxxx) were downloaded from the PDB database. Auto Dock tool (ADT) was employed to prepare proteins (Trott and Olson, 2010). The 3D structure of the studied compound (MOQTA) was obtained using a *CIF* file. And acarbose was used as a reference drug for comparison in the *in vitro* study. Docking grids box was established to cover the catalytic nucleophile and acid/base sites assigned to D518 and D616, respectively (Hermans, 1991; Roig-Zamboni, 2017) And were prepared using Auto Grid with a spacing of 0.375 Å and dimensions 70; 42; 70 Å (x = -11.303; y = -30.54; z = 93.287) and 64; 42; 46 Å (x = 5.024; y = 13.128; z = 60.575) respectively for α-amylase and α-glucosidase. The grids were created around the enzyme active site. Docking was performed using

Table 1 Refined crystal data for MOQTA.

Value	Parameter
Chemical formula	$C_{21}H_{20}N_6O_2$
Crystal system, space group	Monoclinic, $P2_1/n$
Temperature (K)	150
a, *b*, *c* (Å)	7.1831 (7), 18.8662 (17), 13.6756 (12)
β (°)	96.113 (1)
V (Å^3)	1842.7 (3)
Z	4
Radiation type	Mo *K*a
μ (mm^{-1})	0.10
Crystal size (mm)	0.27 × 0.25 × 0.20
Absorption correction	Multi-scan
	TWINABS (Sheldrick, 2009) (Sheldrick, 2009)
T_{min}, T_{max}	0.97, 0.998
No. of measured, independent and observed [$I > 2\sigma(I)$] reflections	53140, 53140, 39,130
R_{int}	0.042
$(\sin\theta/\lambda)_{max}$ (Å^{-1})	0.668
$R[F^2 > 2\sigma(F^2)]$, $wR(F^2)$, *S*	0.053, 0.145, 1.07
No. of reflections	8723
No. of parameters	265
No. of restraints	2
H-atom treatment	H-atom parameters constrained
$\Delta\rho_{max}$, $\Delta\rho_{min}$ (e Å^{-3})	0.29, −0.22

AutoDock Vina and employed the Lamarck Genetic Algorithm (LGA) and the Solis and Wets search methods. Other docking parameters were set at their default values. The best docking poses for the studied compound were visually analyzed using Discovery Studio 4.5. The docking procedure was first validated by re-docking the 1-DEOXYNOJIRIMYCIN and 3,5,7-TRIHYDROXY-2-(3,4,5 -TRIHYDROXYPHENYL)-4H-CHROMEN-4-ONE successively into its binding site of the crystal structure of the α-glucosidase and α-amylase enzyme.

3. Result and discussion

The preparation of MOQTA was described in Scheme1. The starting material, MQO was made by treating *o*-phenylenediamine with ethyl pyruvate in chloridric acid 4.4 N. MOQTA shows a good synthon for various pharmacologically active compounds (Ramli et al., 2010). The lactam function of MQO is very reactive, so it is condensed by alkylation with propargyl bromide to afford the dipolarophile MPO. An example, it is used to synthesize 1,2,3-triazole. With an intense dipole moment, this scaffold could actively participate in hydrogen bonding and π -stacking interactions (Ferreira et al., 2010); π-stacking, hydrogen bonding and hydrophobic effect play critical roles in promoting both enzymes' inhibitory activity (Liu et al., 2007; Li et al., 2011). Due to the importance of the 1;2;3 -triazole and *N*-arylacetamide moieties in the therapeutic area and have suitable inhibitory activities towards α-amylase and α-glucosidase (Ye et al., 2019; Wang et al., 2016; Wang et al., 2017), it seems interesting to associate these heterocycles with the 3-methylquinoxalin-2-one derivative MPQ. Thus, we have studied the copper-catalyzed 1,3-dipolar cycloaddition reaction of 2-azido-*N*-phenylacetamide and the compound MPO. The structures of MPQ and MOQTA were elucidated based on spectral data.

*3.1. 3-methyl-1-(prop-2-yn-1-yl)quinoxalin-2(1H)-one (**MPQ**)*

Yield 73%, FT-IR (ATR, υ, cm^{-1}): 1264.90 υ (N-C_{amide}), 1650.10 υ (C = O_{amide}), (1571.54–1598.51) υ(C = C_{arom}), (1051.91–1265.29) υ(C-H_{arom}), 2114 υ (C≡C $_{propargyl}$). ^{1}H NMR (chloroform-d) δ ppm: 2.6 (3H, s,CH_3); 2.3 (1H, s, CH); 5.1 (2H,s, CH_2); [7.2–7.8] (4H, m, CH_{arom}); ^{13}C NMR (chloroform-d) δ ppm: 21.6 (CH_3); 31.6 (CH_2); 75.6 (CH); 78.5 (C≡$C_{propargyl}$); 157.58 (C = $O_{quinoxaline}$).

*3.2. 2-(4-((3-methyl-2-oxoquinoxalin-1(2H)-yl)methyl)-1H-1,2,3-triazol-1-yl)-N- (p-tolyl)acetamide (**MOQTA**)*

Yield 66%, mp = 222.7–224.5 °C, FT-IR (ATR, υ, cm^{-1}): (636.86–675.05) υ(C-$H_{CH3qinoxaline}$), 951.46 υ(CH_2), (1057.91–1369.13) υ(C-H_{arom}), 1307 υ(N = $N_{triazole}$), 1362.13 υ(N-$H_{acetaamide}$), (1423.31–1467.21) υ(CH_3 $_{Tolylacetaamide}$), (1509.78–1534) υ(C = C_{arom}), 1661.85 υ(C = O $_{amide}$), 1701.38 υ(C = $O_{acetaamide}$); ^{1}H NMR (DMSO d_6) δ ppm: 5.55 (2H, s, CH_{2qui}); 5.26 (2H, s, $CH_{2triazol}$); 8.1 (1H, s, $CH_{Triazol}$); 11.37 (1H, s, NH); 2.5 (3H, s, CH_3 $_{quinoxaline}$); 2.26 (3H, s, CH_{3tolyl}); 6.48–7.79 (m, J = 7.5 Hz, 13H_{Ar}); ^{13}C NMR (DMSO d_6) δppm: 37.30 (CH_2-N_{Quin}); 52.13 (CH_2-$N_{Triazol}$); 21.17 (CH_3 $_{Quin}$); 20.40 (CH_3); 129.24 ($CH_{Triazol}$); 165 (C = O $_{amid}$); 157.58 (C = O $_{quinoxaline}$); HRMS (ESI-MS) (m/z) calculated for $C_{21}H_{20}N_6O_2$ 388,16 found 389.16.

The ^{1}H NMR spectrum of MPQ revealed three signals at δ 2.59, 2.27, and 5.04 ppm due to the methyl of quinoxaline, CH of propargyl group, and CH_2 attached to the quinoxaline nitrogen, respectively. Confirming the alkylation reaction of 3-methylquinoxaline MQO with propargyl bromide. Also, ^{1}H NMR shows the signals relating to aromatic protons between 7.24 and 7.81 ppm. (Abad et al., 2020).

^{1}H NMR spectrum of the title compound MOQTA, exhibited five signals at δ 2.26, 5.26, 5.55, 8.1, and 11.37, referring to CH_3 tolyl group, CH_2 triazole adjacent, CH_2 quinoxaline adjacent, CH of triazole group and NH of acetamide group, respectively. It also revealed the absence of signals at δ 3.3 et 5.1 ppm corresponding to the propargyl hydrogen, which confirms the cycloaddition reaction between MPQ and the azide ATA. The ^{13}C NMR spectrum presented signals at δ at 20.40, 37.30, 52.13, 129,24 and 165 ppm referring to CH_3 of tolyl group, CH_2 triazol adjacent, CH_2 quinoxaline adjacent, CH of triazole group and carbon of acetamide, respectively. Furthermore, in addition to the presence of the CH_3 quinoxaline signal at 21.17 ppm. IR spectrum of MOQTA revealed a band at 1308.19 cm^{-1} for the N = $N_{triazole}$, a band at 1362.13 cm^{-1} for the NH group and an absorption band at 1769.6 cm^{-1} characteristics for the carbonyl group. These data are in agreement with the characteristics of the analogous compounds of MOQTA (Abad et al., 2020; Missioui et al., 2022). Its mass spectrum demonstrated a molecular ion peak (MH^+, m/z = 389.16) which conforms to $C_{21}H_{20}N_6O_2$.

3.3. X-ray crystallography

As indicated by the 1.33(10)° dihedral angle between the constituent planes, the quinoxaline unit is not planar. The dihedral angle between the C1/C6/N1/C7/C8/N2 and N3/N4/N5/C11/C12 planes is 88.77(10)° while that between the latter ring and the C15···C20 ring is 89.97(5)° giving the molecule an approximate "U"-shaped conformation. The orientation of the C15···C20 ring is partially determined by the weak, intramolecular C16 –H16…O2 interaction (Table 2 and Fig. 1). The bond lengths and interbond angles appear as expected for the given formulation.

In the crystal, N6—H6···N5 H-bonds with graph sets C1,1(7) form chains of molecules extending along the *a*-axis direction which are linked into layers parallel to the *ac* plane by C13—H13B···O1 H-bonds having graph sets C1,1(9). These interactions are reinforced by weaker C10—H10A···O2, C19—H19···O2 and C20—H20···O2 hydrogen bonds having graph sets C1,1(8), C1,1(7) and C1,1(6), respectively plus) C3—H3···Cg4 interactions (Table 2 and Fig. 2). Each layer has an inversion-related counterpart which is linked to it via C12—H12···N1 hydrogen bonds (graph sets C1,1(9)) and slipped π-stacking interactions between quinoxaline units (centroid···centroid = 3.5495(12) Å, dihedral angle = 1.33°) Table 2 and Fig. 3). The layers are connected by C4—H4···N4 hydrogen bonds with graph sets C1,1(10) (Table 2 and Fig. 4).

Table 2 H-bond geometry (Å, °).

D—H···*A*	*D*—H	H···*A*	*D*···*A*	*D*—H···*A*
N6—H6···N5^{i}	0.91	2.25	3.142 (2)	165
C3—H3···Cg4^{ii}	0.95	2.69	3.516 (2)	146
C4—H4···N4^{iii}	0.95	2.53	3.356 (3)	145
C9—H9C···Cg2^{iv}	0.98	2.61	3.364 (2)	134
C10—H10A···O2^{v}	0.99	2.57	3.439 (2)	146
C12—H12···N1^{iv}	0.95	2.54	3.379 (3)	147
C13—H13B···O1^{vi}	0.99	2.37	3.174 (2)	138
C16—H16···O2	0.95	2.28	2.868 (3)	120
C19—H19···O^{2i}	0.95	2.55	3.157 (3)	122
C20—H20···O^{2i}	0.95	2.52	3.133 (3)	123

Symmetry codes: (i) x − 1, y, z; (ii) x + 1, y, z; (iii) − x + 3/2, y + 1/2, −z + 1/2; (iv) − x + 1, −y + 1, −z + 1; (v) x + 1/2, −y + 1/2, z + 1/2; (vi) x − 1/2, −y + 1/2, z − 1/2.

3.4. Computational ad theoretical study

3.4.1. Geometric optimization of MOQTA

The optimized molecular parameters of the molecule using DFT/B3LYP/6–311 + + G(d,p) method and X-ray data for bond angles and bond distances were given in Table 3 and Table 4, respectively. For bond distances, the error values range up to 0.0241 Å. While the significant error was found for N4—N5 bond distance with 0.0241 Å, whereas the smallest error was found for C10—C11 bond distance. It can be considered the theoretical results are consistent with the experimental results.

For bond angles, the biggest difference between X-ray and optimized data was calculated for C14-N6-C15 bond angle with −2.0926° error value. The lowest error value belongs to C5-C4-C3 bond angle with 0.0098°. Like bond distances, bond angles calculated by the DFT method are close to experimental values.

3.4.2. Molecular Electrostatic map

Molecular Electrostatic Potential (MEP) map of the MOQTA was generated by DFT/B3LYP/6–311 + + G(d,p) basis set and given in Fig. 5. MEP reveals electrophilic and nucleophilic centers and helps us understand non-bonding interactions (Hathwar et al., 2015; Okulik and Jubert, 2005; Luque et al., 2000). In the MEP, while the red areas show electrophilic attack centers, the blue areas show nucleophilic attack centers (Scrocco and Tomasi, 1978). It can be seen that the electrophilic centers in the MEP are in the vicinity of the oxygen and nitrogen atoms. These values are −0.0510 a.u. for O1 atom, −0.0417 a.u., for O2 atom, −0.0383 a.u. for N1 atom and −0.0461 a.u. for the region between N4 and N5 atom. The most nucleophilic region was detected at the vicinity of H6 atom with + 0.0709 a.u. The crystal structure contains intermolecular N6—H6N5, C4—H4N4, C10—H10AO2, C12—H12N1, C13—H13O1, C19—H19O2, C20—H20O2 hydrogen bonds and intramolecular C16—H16O2 hydrogen

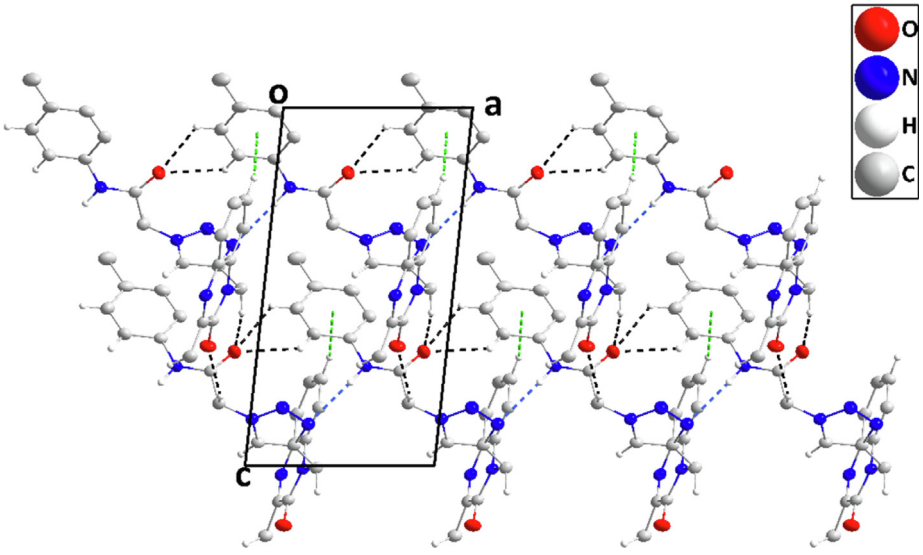

Fig. 2 Detail of a portion of two chains seen along the *b*-axis direction. N—H···N, and C—H···O H-bonds are depicted, respectively, by blue and black dashed lines. C—H···π(ring) interactions are depicted by green dashed lines.

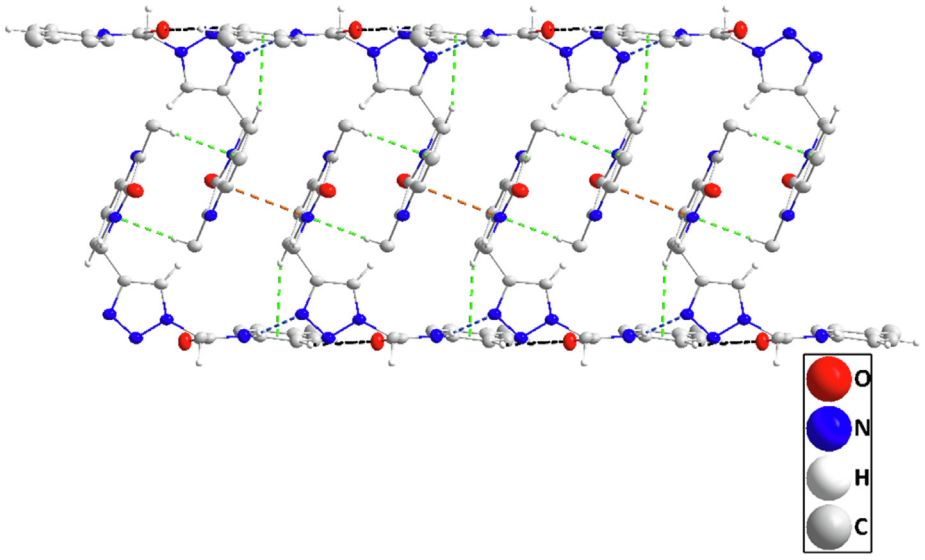

Fig. 3 Detail of portions of two inversion-related layers projected on $\left(01\bar{1}\right)$ showing the π-stacking interactions (orange dashed lines). C—H···π(ring) interactions and C—H···O hydrogen bonds are depicted, respectively, by green and black dashed lines.

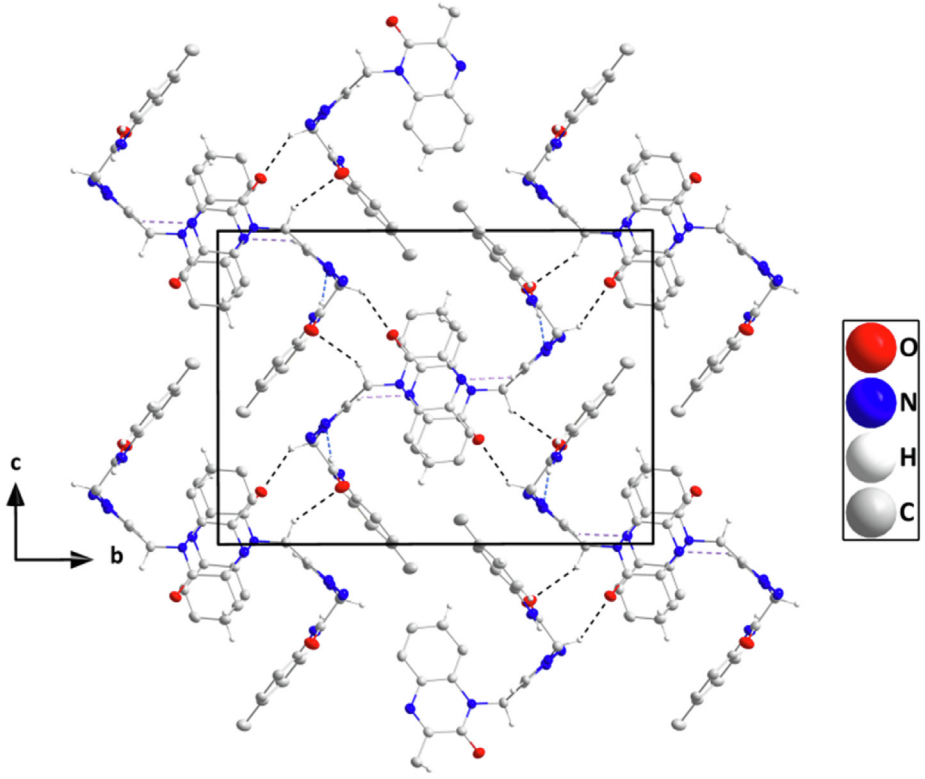

Fig. 4 Packing seen along the *a*-axis direction giving an end view of several chains and their linkage through C—H···O hydrogen bonds (black dashed lines). π-stacking and C—H···π(ring) interactions are omitted for clarity.

Table 3 Experimental and theoretical bond distances of MOQTA (Å).

Bond Distances							
Atoms	**X-ray**	**DFT**	**Error**	**Atoms**	**X-ray**	**DFT**	**Error**
O1-C8	1.226(2)	1.2276	−0.0016	N1-C6	1.390(2)	1.3834	0.0066
N1-C7	1.298(2)	1.2915	0.0065	N2-C1	1.401(2)	1.3949	0.0061
N2-C8	1.375(2)	1.3886	−0.0136	N3-N4	1.341(2)	1.3546	−0.0136
N2-C10	1.476(2)	1.4757	0.0003	N3-C13	1.455(2)	1.4498	0.0052
N3-C12	1.348(2)	1.3538	−0.0058	N5-C11	1.364(2)	1.3641	−0.0001
N4-N5	1.323(2)	1.2989	0.0241	N6-C15	1.426(2)	1.4179	0.0081
N6-C14	1.347(2)	1.3661	−0.0191	C1-C2	1.391(3)	1.4045	−0.0135
C1-C6	1.409(3)	1.4149	−0.0059	C2-C3	1.379(3)	1.3874	−0.0084
C7-C9	1.488(3)	1.4977	−0.0097	C3-C4	1.387(3)	1.4006	−0.0136
C10-C11	1.497(3)	1.497	0	C4-C5	1.379(3)	1.3833	−0.0043
C15-C20	1.386(3)	1.3986	−0.0126	C5-C6	1.396(3)	1.4042	−0.0082
C16-C17	1.387(3)	1.3919	−0.0049	C7-C8	1.487(3)	1.4856	0.0014
C17-C18	1.386(3)	1.3986	−0.0126	C11-C12	1.364(3)	1.3783	−0.0143
C18-C19	1.390(3)	1.3977	−0.0077	C13-C14	1.526(3)	1.5401	−0.0141
C19-C20	1.385(3)	1.3903	−0.0053	C15-C16	1.393(3)	1.3995	−0.0065
O2-C14	1.216(2)	1.2163	−0.0003	C18-C21	1.507(3)	1.5093	−0.0023

Table 4 The experimental and theoretical bond angles of the MOQTA (°).

Bond Angles					
Atoms	**X-ray**	**DFT**	**Atoms**	**X-ray**	**DFT**
C7-N1-C6	118.86(16)	119.4641	C19-C20-C15	120.3(2)	120.4785
C8-N2-C10	117.96(16)	116.4543	C8-N2-C1	121.83(16)	121.8952
N4-N3-C12	111.22(16)	110.8914	C1-N2-C10	120.20(16)	121.6489
C12-N3-C13	128.38(17)	129.8309	N4-N3-C13	120.09(16)	119.2652
N4-N5-C11	108.52(16)	109.4753	N5-N4-N3	106.98(15)	107.2333
C2-C1-N2	122.54(17)	122.8732	C14-N6-C15	126.89(17)	128.9826
N2-C1-C6	117.97(17)	117.6003	C2-C1-C6	119.48(18)	119.5256
C2-C3-C4	121.14(19)	121.1275	C3-C2-C1	119.91(19)	119.6938
C4-C5-C6	120.65(19)	120.7363	C5-C4-C3	119.45(19)	119.4402
N1-C6-C1	122.02(17)	122.0814	N1-C6-C5	118.61(17)	118.4638
N1-C7-C8	123.44(18)	123.2729	C5-C6-C1	119.36(18)	119.4542
C8-C7-C9	116.44(17)	116.3535	N1-C7-C9	120.12(17)	120.3735
O1-C8-C7	121.79(18)	122.6526	O1-C8-N2	122.56(18)	121.8852
N2-C10-C11	112.40(15)	114.019	N2-C8-C7	115.65(17)	115.4554
N5-C11-C12	108.55(17)	108.2603	N5-C11-C10	121.18(17)	121.7624
C12-C11-C10	130.27(18)	129.976	N3-C12-C11	104.73(17)	104.1396
N3-C13-C14	110.25(15)	111.9846	O2-C14-C13	120.37(18)	120.6494
O2-C14-N6	125.25(19)	125.5932	C20-C15-C16	119.29(19)	119.2427
N6-C14-C13	114.37(17)	113.7077	C16-C15-N6	123.26(18)	123.4533
C20-C15-N6	117.41(18)	117.3039	C18-C17-C16	122.3(2)	122.2655
C17-C16-C15	119.3(2)	119.3124	C17-C18-C21	121.6(2)	121.0374
C17-C18-C19	117.3(2)	117.4913	C20-C19-C18	121.5(2)	121.2089
C19-C18-C21	121.1(2)	121.4692			

bonds. This is a sign that all electrophilic and nucleophilic attack centers participate in hydrogen bonds.

3.4.3. Hirshfeld surface analysis (HSA)

HSA and 2D fingerprint plots were created using Crystal Explorer 3.0 computer program and Hirshfeld surfaces of the molecule with the normalized contact distance (d_{norm}) was given in Fig. 6. The d_{norm} can take negative and positive values according to intermolecular contacts are closer or longer than VDW radii, respectively. In the Hirshfeld surface negative values are given by red areas, and positive values are presented by blue areas. d_{norm} range from 0.366 Å to 1.258 Å.

In Fig. 5, the Hirshfeld surface of the molecule with adjacent molecules is given. Fig. 6 **(a)** represents intermolecular N6—H6···N5, C12—H12···N1, C19—H19···O2 and C20—H20···O2 interactions between the central molecule and adjacent molecules, Fig. 6 **(b)** represents intermolecular C4—H4···N4 hydrogen bond between the central molecule and adjacent molecules, Fig. 6 **(c)** represents intermolecular C10—H10A···

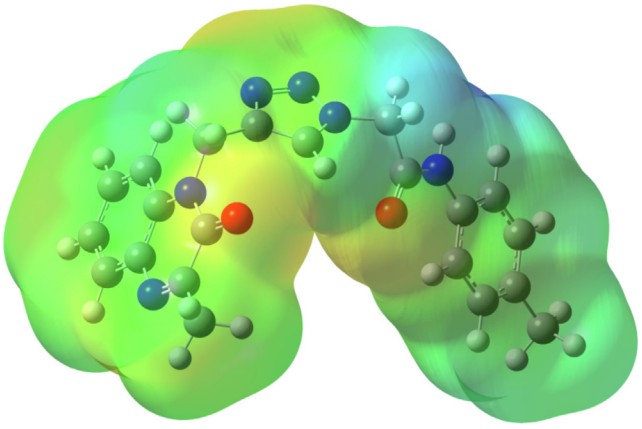

Fig. 5 The Molecular Electrostatic Potential (MEP) map of MOQTA.

O2 and C13—H13B···O1 interactions between the central molecule and adjacent molecules. In the Hirshfeld surface, the environment of C4—H4, C10—H10A, C12—H12, C13—H13B, C19—H19, C20—H20, N6—H6 groups and N1, N4, N5, O1, O2, atoms are seen like red areas that these regions are active regions for intermolecular interactions. X-ray diffraction results show that intermolecular N6—H6N5, C4—H4N4, C10—H10AO2, C12—H12N1, C13—H13BO1, C19—H19···O2, C20—H20O2 hydrogen bonds are present in these regions.

In Fig. 7, OH, HO, NH and HN interactions and the 2D fingerprint plot with hydrogen bonds were given and it is seen that OH / HO and NH / HN interactions in the 2D fingerprint plot are seen like two distinct spikes. While the spikes in the lower right and upper left of the 2D fingerprint plot correspond to NH / HN interactions resulting from intermolecular C12—H12···N1, C4—H4···N4 and N6—H6···N5 interactions. The spikes in the middle right and middle left of the 2D fingerprint plot correspond to OH/ HO interactions resulting from intermolecular C10—H10A···O2, C13—H13BO1, C19—H19···O2, C20—H20O2 hydrogen bonds. The contributions of these interactions are 12.1% and 15.8% to the Hirshfeld surface, respectively.

Fingerprint plots of crystal and dominant interactions can be seen in Fig. 8. In the 2D fingerprint plot, characteristic wings at the top of left and bottom of right are defined like C-Hπ interactions (Seth et al., 2011; Luo and Sun, 2013). As shown in Fig. 8, while the upper left wing corresponds to the spots in the vicinity of C-H donor, the lower right wing corresponds to the spots in the vicinity of π acceptor. The crystal structure has C3—H3π, C9—H9Cπ interactions and the contribution of C···H / H···C interactions is 18.5% to Hirshfeld surface. H-H contacts with 44.7% give the most dominant contribution to the Hirshfeld surface. The contributions of intermolecular interactions with rations to the total Hirshfeld surface were given in Table 5.

3.4.4. Frontier Molecular orbitals

Frontier molecular orbitals (FMOs) play an essential role in molecular orbitals in chemical, electrical, and optical properties (Fleming and Wiley, 1979). Highest Occupied Molecular Orbital (HOMO) and Lowest Unoccupied Molecular Orbital (LUMO) from these orbitals are very important for the biological activities of molecules. Because of charge transfer, while a small energy gap between HOMO and LUMO increases the biological activity of molecules, low energy gap decreases the biological activity of molecules (Yousef et al., 2016; Agrawal et al., 2016; Wu et al., 2020; Pearson, 2005). According to Koopmans' theorem (Koopmans, 1934), ionization potential, I, and electron affinity, A, are given by.

$$I = -E_{HOMO} \text{and} A = -E_{LUMO} \quad (1)$$

Chemical hardness, η, is defined as the resistance of chemical potential against to change electron number (Pearson, 2005; Parr and Pearson, 1983) and is defined in terms of ionization potential and electron affinity.

$$\eta = \frac{1}{2}(I - A) \quad (2)$$

While soft molecules have a low energy gap, hard molecules have high energy gap (Fleming and Wiley, 1979).

Therefore, FMOs were created using DFT with B3LYP/6–311 + + G(d,p) basis set and are given in Fig. 9**.** In molecule, HOMO and LUMO orbitals are mainly concentrated on 3-methylquinoxalin-2(1H)-one part of a molecule. While HOMO-1 orbitals are concentrated on N-p-tolylformamide group, LUMO + 1 orbitals are concentrated on 2-(4,5-dihydro-1H-1,2,3-triazol-1-yl)-N-(p-tolyl)acetamide group of the molecule. The energy gap between LUMO and HOMO orbitals is 4.3824 eV, too.

3.5. Biological activity

3.5.1. Antidiabetic activity

The *in vitro* antidiabetic activity of hybrid quinoxaline derivative MOQTA was screened for two enzymes inhibitory properties. Effects were compared with acarbose. The obtained results proved that the MOQTA has an inhibitory effect on the digestive enzymes, as shown in Table 6. The results showed that MOQTA had an average inhibitory effect on α-glucosidase activity (**IC_{50} 288.6 ± 0.965 μM**), which exceeds

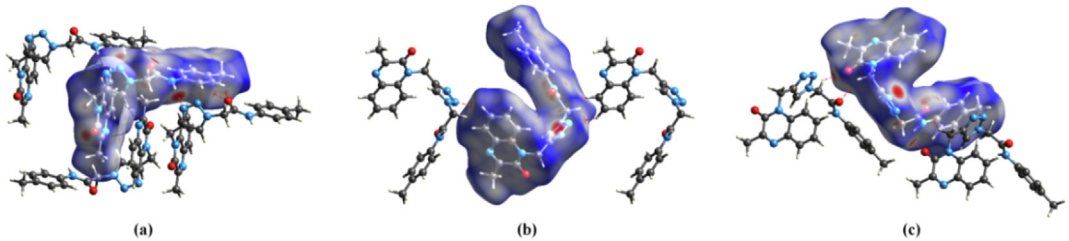

Fig. 6 Hirshfeld surface with intermolecular hydrogen bonds.

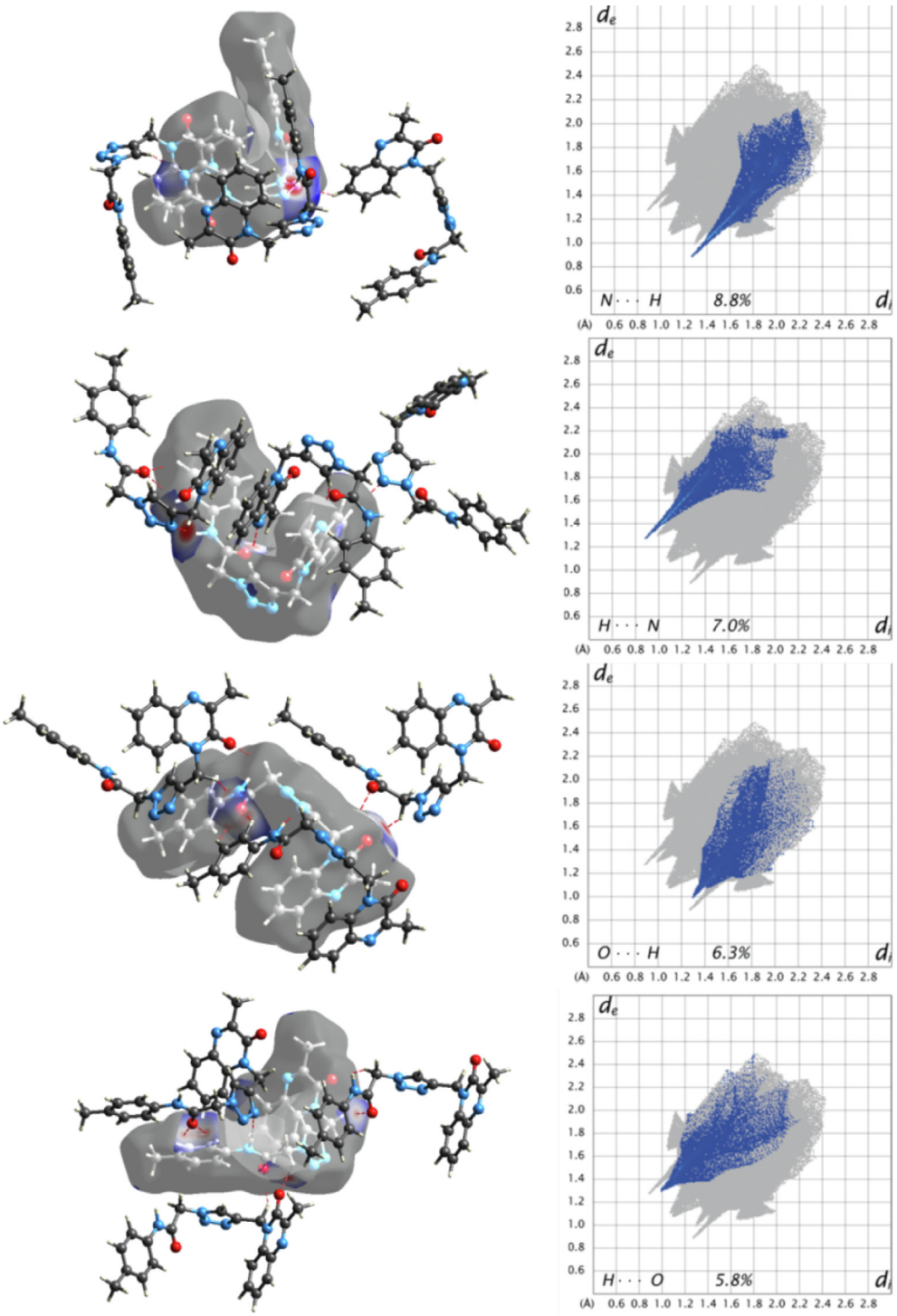

Fig. 7 2D fingerprint plot and 3D Hirshfeld surface mapped with d_{norm} with the intermolecular interactions between the molecule and neighbor molecules.

the acarbose taken as a reference with IC_{50} value was activity (**IC_{50} 72.58 ± 0.682 μM**). MOQTA is a statistically highly significant as $P < 0.001$, a similar result was found for α-amylase. Table 6 demonstrated an excellent activity (**IC_{50}246.6 ± 1.16 μM),** which exceeds the acarbose taken as a reference **(IC_{50} 115.6 ± 0.574 μM).** Therefore, it is considered an active compound.

Values represent mean ± standard deviation (n = 3).

3.5.2. Antioxidant activity

The antioxidant activity of MOQTA complex was evaluated *in vitro* using radical methods, ABTS, DPPH, FRAP and H_2O_2. The antioxidant property of MOQTA was assessed in comparison with ascorbic acid as standard. The obtained result of DPPH assay showed good antioxidant activity, with IC_{50} value (101 ± 1.01 μM), similar to the action of NPOQA, a novel *N*-arylacetamides quinoxaline-based compound

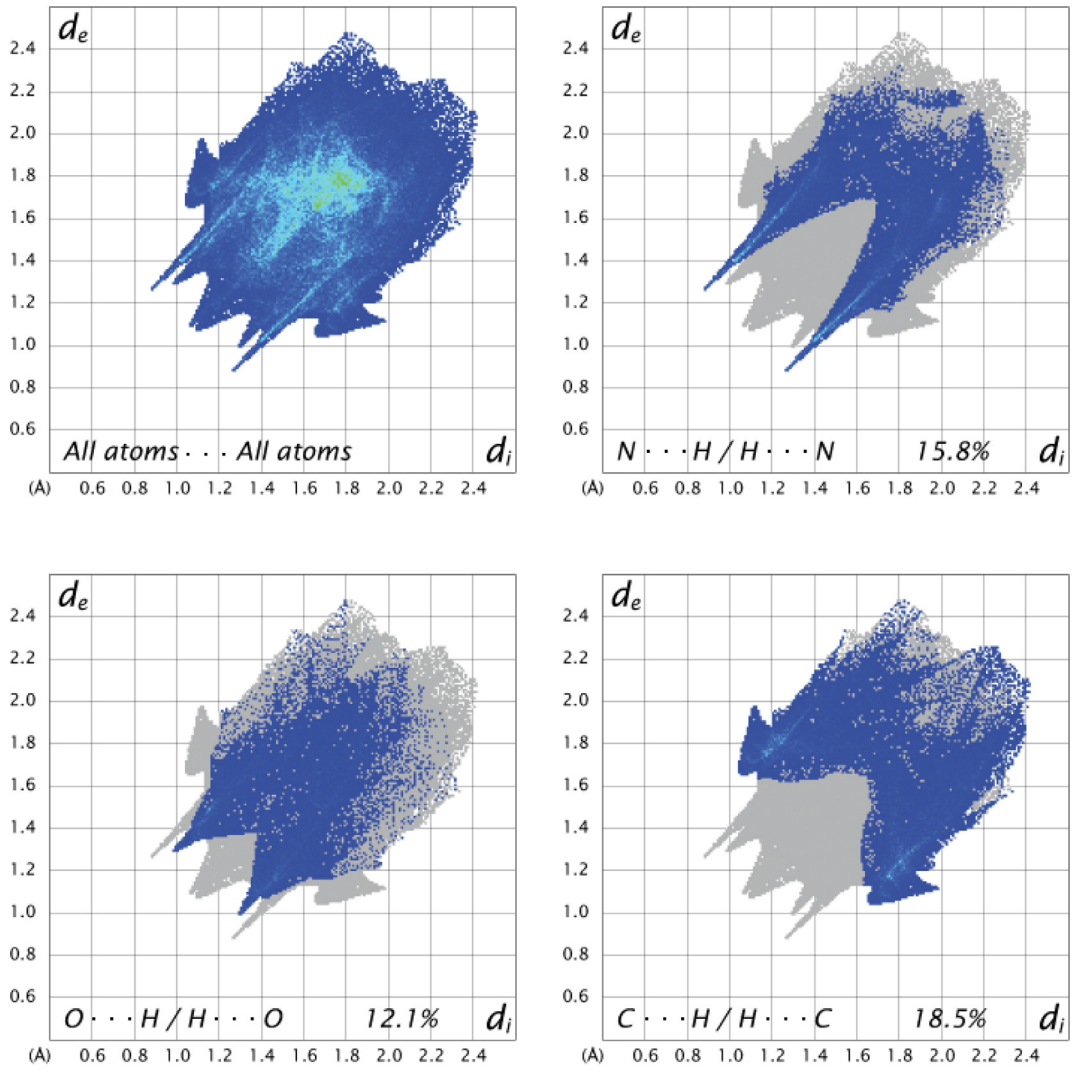

Fig. 8 2D fingerprint plot of All atoms···All atoms, N···H / H···N, O···H / H···O, C···H / H···C interactions.

Table 5 The contributions of short contacts to Hirshfeld Surface of MOQTA (%).

H···H	C···H	N···H	O···H	C···C	C···N	C···O	N···O	N···N
44.7	18.5	15.8	12.1	3.9	3.3	1.2	0.3	0.2

recently reported (Missioui et al., 2021). While IC_{50} value of ascorbic acid (78.11 ± 0.68 µM). In the ABTS test, MOQTA has developed an important antioxidant activity compared to the activity of NPOQA (Fig. 10) (Missioui et al., 2021). The antioxidant activity presented in the DPPH test, Table 7**,** displayed the average antioxidant ability (59.61 ± 0.65 µM). Furthermore, the FRAP method observed the highest reducing power for MOQTA (133,9 ± 0,52 µM)**.** The synthesized compound MOQTA demonstrated activity in H_2O_2, with IC50 value (44.83 ± 1.32 ± µM), while IC50 value of ascorbic acid (7.45 ± 1.11 µM).

3.6. Molecular docking results

Molecular docking aims to predict the binding types of the studied compound against α-amylase enzymes and α-glucosidase. Docking studies have been reported in previous studies where many compounds were docked with the α-glucosidase/amylase enzymes (Missioui et al., 2021). The docking study of MOQTA and acarbose (standard) is represented in Fig. 11, 12, 13. The binding energy of the compounds and implicated residues of α-glucosidase and α-amylase are shown in Table 8. The results showed that both MOQTA and stan-

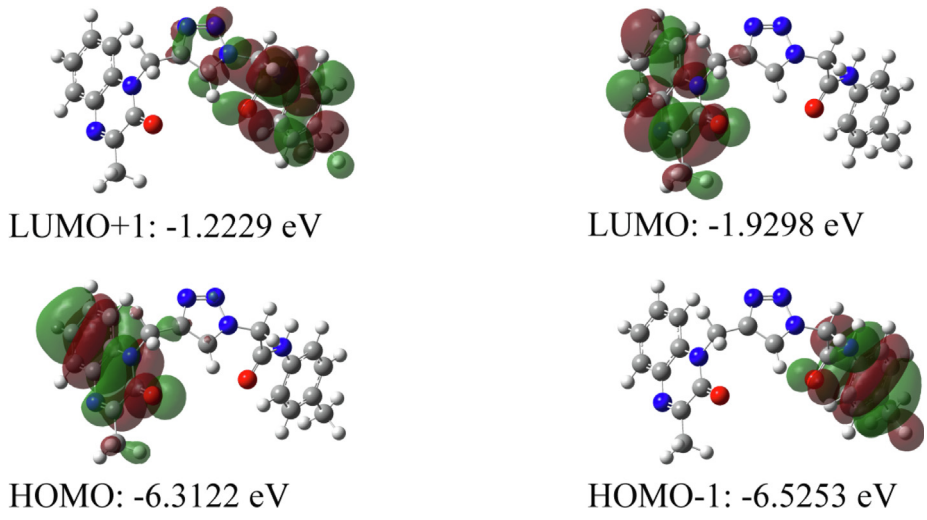

Fig. 9 Frontier molecular orbitals of the compound.

Table 6 IC_{50} of the MOQTA enzyme inhibitory activity.

	(IC_{50} μmol/ml)	
	α-glucosidase	**α-amylase**
MOQTA	288.6 ± 0.965****	246.6 ± 1.1****
NPOQA	83.78 ± 0.888	199.7 ± 0.952 (Missioui et al., 2021)
Standard	72.58 ± 0.682	115.6 ± 0.574

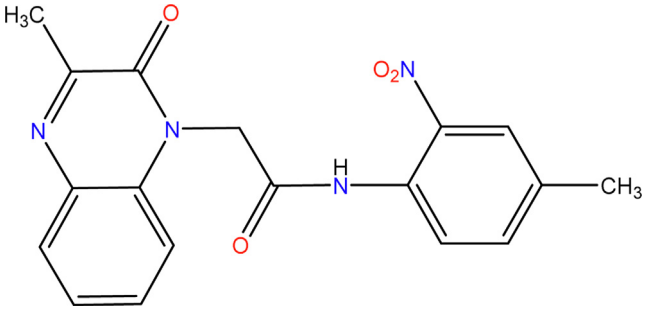

Fig. 10 The structure of NPOQA.

dard were able to bind to the active site of α-glucosidase, the calculated binding energy was found to be −7.5 and −6.5 kcal/-mol successively for MOQTA and standard (Table 8), significantly improved compared to the binding affinity of NPOQA (Missioui et al., 2021). MOQTA showed three hydrogen bonds interactions with the main chains of residues SER 566, ARG 189, TYR191 as appeared in Fig. 11 and stabilized in the active site pocket with hydrophobic interactions with residues LEU565, ASP243, ARG190, and TYR191. Many H-bonded interactions were formed between different hydroxyl groups of acarbose and amino acids Arg252, Pro312, Ser3, Arg421, Gly403, Arg398, Thr11, Arg5, Asn5, and Gly334 of the α-glucosidase enzyme (Fig. 13). The studied compound MOQTA and standard shear the same hydrophobic interactions with α-glucosidase residues arg190, which may explain the crucial binding affinity compared to the standard drug acarbose.

We have also performed a docking study of MOQTA and the standard with α-amylase. The calculated binding affinity was predicted to be-7.7 and −6.6 Kcal/mol successively for MOQTA and acarbose, as shown in Table 8, which is better than the binding affinity of NPOQA (Missioui et al., 2021). Compound MOQTA occupied the hydrophobic pocket of the enzyme and showed two hydrogen bonds interactions with residues PRO332 SER289 and several other types of interactions with residues HIS331 PRO4 PHE335 ASP 402. Interactions analysis showed that the formed ring 1,2,3-triazole allowed the studied compound to establish strong N…H hydrogen interactions, which is consistent with the literature (Ferreira et al., 2010); Consequently, the formation of a stable complex ligand-receptor with a low free energy ΔG (Fig. 11). The comparison of the obtained results with the binding of NPOQA (Missioui et al., 2021) showed an increase of affinity between ligand and studied enzyme that can also be allowed to the heterocyclic structure of triazole.

Table 7 Tests (ABTS, FRAP, H_2O_2 and DPPH) of MOQTA. Data are expressed as mean ± SD (n = 3).

IC_{50} μM)	**DPPH**	**ABTS**	**FRAP**	**H_2O_2**
MOQTA	101 ± 1.01	59.61 ± 0.65	133.9 ± 0.52	44.83 ± 1.32
NPOQA	104 ± 4.65	330.30 ± 3.44	298.54 ± 6.59	5.06 ± 0.48 (Missioui et al., 2021)
Ascorbic Acid	78.11 ± 0.68	22.49 ± 0.59	88.12 ± 0.23	7.45 ± 1.11

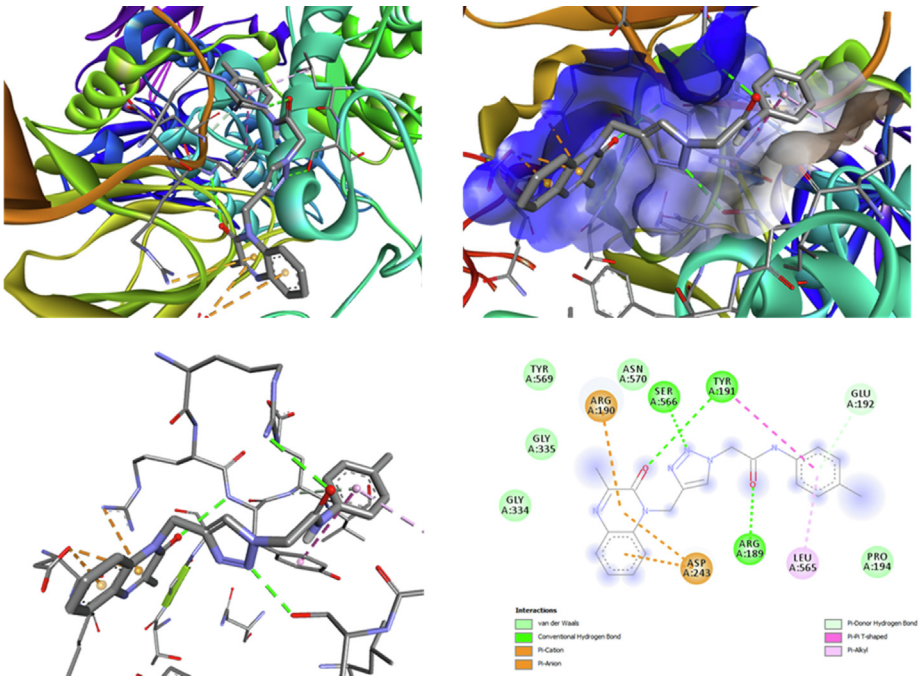

Fig. 11 The ligand MOQTA is docked into the binding site of glucosidase. (A) Binding of MOQTA with glucosidase, (B) (3D) amino acid residues and interactions in MOQTA-glucosidase hydrophobic pocket. (C) (3D) amino acid residues and interactions in MOQTA-glucosidase complex. (D) (2D) amino acid residues and many interactions formed in MOQTA-glucosidase compound.

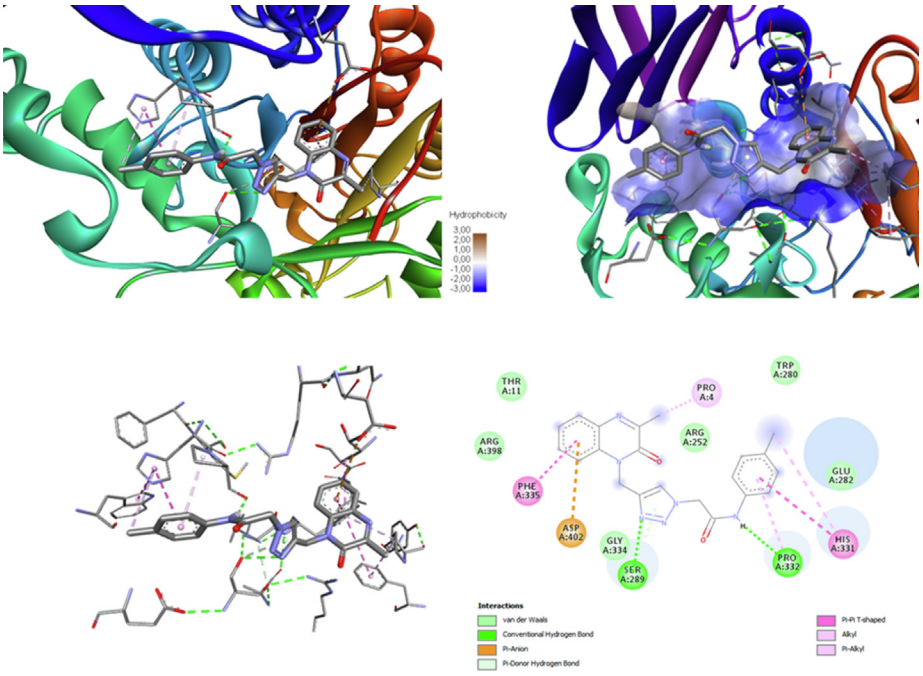

Fig. 12 The ligand MOQTA is docked well into the binding site of amylase. (**A**) The interaction of MOQTA with amylase, (**B**) (3D) amino acid residues interactions in acarbose-amylase hydrophobic pocket. (**C**) (3D) amino acid residues and interactions in MOQTA-amylase complex. (**D**) (2D) amino acid residues and interactions formed in MOQTA-amylase.

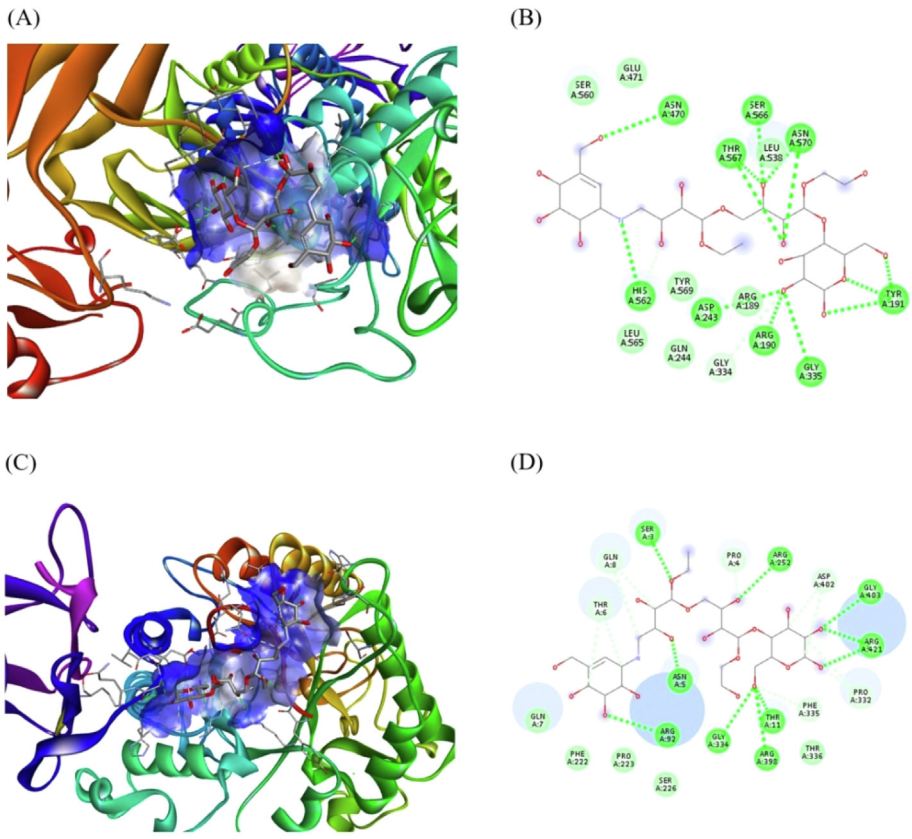

Fig. 13 Acarbose was docked with –amylase and glucosidase. (**A**) A display of binding of acarbose with glucosidase (**B**) amino acid residues and interactions in Acarbose-glucosidase complex, (**C**) A display of binding acarbose with -amylase (**D**) A display of amino acid residues and interactions formed in acarbose-amylase complex.

Table 8 The binding energy for the MOQTA and acarbose.

	α-Glucosidase		α-Amylase	
	Affinity kcal/mol	**Residues**	**Affinity kcal/mol**	**Residues**
Standard	−6.5	THR567, ASN570, SER566, HIS562,, LEU538, ASN470, GLY335, ASP243, ARG190, TYR191, ARG189	−6.6	ARG421, GLY403, ASP402, ARG252, GLN8, THR6, PRO4, SER3 PRP332, PHE335, THR336, THR11, ARG398, GLY334, ASN5, ARG92
NPOQA	**−6.9**	LEU538, ASP243, ASN570, TYR191, SER566, THR56	**−7.6**	PRP332, PHE335, THR336, THR11, ARG398, GLY334, ASN5, ARG92ASP402,ARG398, SER289, TYR333, ARG421, PRO332
MOQTA	**−7.5**	LEU565, ASP243, ARG190, TYR191, TYR191, SER 566, ARG 189	**−7.7**	PRO332 SER289 HIS331 PRO4 PHE335 ASP 402

The binding energy of MOQTA with α-amylase and α-glucosidase is very encouraging. This suggests that MOQTA merits further assessment in the context of *in vitro*/ *in vivo* of α-glucosidase and α-amylase studies.

3.7. Lipinski's rule and ADMET prediction

The Lipinski rule and ADMET parameters(Kerflani et al., 2022; Lipinski et al., 2001) of the investigated molecule were performed using the web servers Swissadme ('SwissADME'. http://www.swissadme.ch/ (accessed Dec. 15, 2021) and ADMETlab2.0 ('ADMETlab 2.0′. https://admetmesh.scbdd.com/ (accessed Sep. 24, 2021), respectively. The Lipinski rule including molecular weight, number of rotational bonds, number of acceptor hydrogen bonds, number of donor hydrogen bonds and log(P) (Adedotun, 2022) were determined. Molecules that violate more than one of these parameters may have bioavailability problems and a high probability

Table 9 Lipinski's Rule of MOQTA.

Lipinski's Rule						
Compound	Molecular Weight (g/mol)	Lipophilicity (MLogP)	H-bond Donors	H-bond Acceptors	Rule Violations	Drug-Likeness
	< 500	< 5	< 5	< 10	< 2	
MOQTA	388.42	1.85	1	8	0	yes
Pioglitazone	356.4	2.16	2	4	0	yes

Table 10 Physicochemical properties.

Physicochemical descriptor	**Value**
Lipophilicity(LogP)	1.938
Distribution at pH 7.4 (logD)	2.423
Polar Surface Area (PSA)	94.70
Plasma protein binding (PPB)	94.32%

of not being similar to a drug (Ferreira and Andricopulo, 2019).

The server (ADMETlab) was utilized to predict the absorption, distribution, metabolism, excretion, and toxicity (ADMET) properties of MOQTA. Pioglitazone was used as a standard drug.

As observed in Table 9 MOQTA respects all the conditions mentioned in Lipinski's rule with Lipophilicity (MLogP) < 5, H-bond Donors < 5, and H-bond Acceptors < 10. As reported in Table 10, logD value is in the range of 2.423, suggesting a stabilized distribution. Thus, the obtained value of logP 1.938 indicates that the compound may be slightly permeable to the biological barriers of the physiological system but still has lipophilicity estimated as ideal in the intestinal absorption phase. The PSA evaluated at 94.7 presents a good permeability.

The selected molecule has a low BBB (blood–brain barrier penetration), with a MDCK permeability of 2.6e-05 and a Caco-2 permeability value of −4.747 for the metabolism. The MOQTA could inhibit the cytochromes CYP2C19, CYP2C9, and CYP3A4. (Table11). Non-Rat Acute Oral Toxicity effect has been observed.

The molecule satisfied the conditions mentioned in Lipinski's rule and has good ADMET properties; thus, MOQTA could be orally active in humans.

Table 11 ADMET properties of MOQTA.

ADMET prediction	**Value**
Absorption	
HIA	0.005
MDCK Permeability	2.6e-05
Caco-2 Permeability	−4.747
P-glycoprotein inhibitior	0.977
P-glycoprotein substrate	0.011
F20%	0.007
F30%	0.005
Distribution	
PPB	94.32%
VD	0.232
BBB	
Penetration	0.29
Fu	4.345%
Metabolism	
CYP2C19 substrate	
CYP2C19 inhibitor	0.419
	0.786
CYP2C9 inhibitor	0.917
CYP2C9 substrate	0.796
CYP2D6 inhibitor	0.578
CYP2D6 substrate	0.461
CYP3A4 inhibitor	0.67
Excretion	
CL	8.93
^{T}1/2	0.537
Rat Acute Oral Toxicity	0.034

4. Conclusions

Herein, a straightforward synthesis of a new quinoxaline derivative MOQTA is reported. The XRD analysis illustrates that the quinoxaline unit is not entirely planar, as revealed by the dihedral angle between the constituent planes, 1.33 (10)°. The optimized geometry of the molecule was obtained by the DFT method. Both bond distances and bond angles of an optimized molecule are consistent with the experimental values. Based on the theoretical calculation resuls, the oxygen atom is the main reaction site for electrophilic attack and H6 atom is the most important reaction site of the nucleophilic attack. Hirshfeld surface analysis study also confirms the regions which are active for intermolecular interactions. In the 2D fingerprint plot, NH / HN and OH / HO interactions are present like two distinct spikes and CH / HC interactions are seen like the lower right-wing and the upper left wing. The contributions of these interactions to Hirshfeld surface are 15.8% for NH / HN, 12.1% for OH / HO and 18.5% for CH / HC. The data obtained X-ray diffraction show that

N6—H6N5, C4—H4N4, C10—H10AO2, C12—H12N1, C13—H13BO1, C19—H19O2, C20—H20O2 interactions are present in these active regions. The energy gap between LOMO and HUMO orbitals is 4.3824 eV. The compound MOQTA demonstrated moderate anti-diabetic activity and excellent anti-oxidant activity. Besides, molecular docking analyses were carried out to examine the binding mode between MOQTA and the two enzymes, α-glucosidase and α-amylase. Thus, this study explores, theoretical prediction, antidiabetic, antioxidant activities and docking studies of triazole-quinoxaline- *N*-arylacetamide hybrid system for the development of potential multi-functional medicinal candidates. Finally, physicochemical properties, as well as drug-likeness, demonstrated that MOQTA had interesting ADMET properties.

CRediT authorship contribution statement

Mohcine Missioui: . **Salma Mortada:** . **Walid Guerrab:** . **Güneş Demirtaş:** Writing – original draft. **Joel T. Mague:** . **M'hammed Ansar:** Conceptualization, Methodology. **My El Abbes Faouzi:** Supervision. **E.M. Essassi:** Methodology. **Yassin T.H. Mehdar:** Conceptualization, Writing – review & editing. **Faizah S. Aljohani:** Conceptualization, Writing – review & editing. **Musa A. Said:** Conceptualization, Writing – review & editing. **Youssef Ramli:** Conceptualization, Methodology, Writing – review & editing, Supervision.

Declaration of Competing Interest

The authors declare that they have no known competing financial interests or personal relationships that could have appeared to influence the work reported in this paper.

Acknowledgements

Authors would like to thank Mohammed V University and the Ondokuz Mayıs University Research Fund for financial support for this study. The support of NSF-MRI Grant #1228232 for the purchase of the diffractometer and Tulane University for support of the Tulane Crystallography Laboratory is gratefully acknowledged. MAS is also thankful to AvH for its continuous support.

Appendix A. Supplementary material

Supplementary data to this article can be found online at https://doi.org/10.1016/j.arabjc.2022.103851.

References

Y. Ramli, E. M. Essassi, Advances in synthetic approaches, functionnalization and biological properties of quinoxaline derivatives. In: Advances in Chemistry Research Ed. James C. Taylor Nova Science Publishers, New York. 27 (2015) 109–160.

Y. Ramli, A. Moussaif, K. Karrouchi, E. M. Essassi, Pharmacological profile of quinoxalinone. J. Chem. 2014 Article ID 563406 (2014) 1–21. 10.1155/2014/563406.

N. Abad, Y.Ramli, W. Ettahiri, S. Ferfra, E. M. Essassi, Quinoxaline derivatives: syntheses, reactivities and biological properties les derives de la quinoxaline: syntheses, reactivites et proprietes biologiques, J. Mar. Chim. Heterocycl., 19 (2020) 1-12, 10.48369/IMIST.PRSM/jmch-v19i2.22352.

M. Allali and A. Zarrouk T. Laabaissi, F. Benhiba, Z. Rouifi, M. Missioui, K. Ourrak, H. Oudda, Y. Ramli, I. Warad, New quinoxaline derivative as a green corrosion inhibitor for mild steel in mild acidic medium: Electrochemical and theoretical studies, Int. J. Corros. Scale Inhib.8 (2019) 241–256. 10.17675/2305-6894-2019-8-2-6.

H. Lgaz, Y. ELaoufir, Y. Ramli, M. Larouj, H. Zarrok, R. Salghi, A. Zarrouk, A. Elmidaoui, A. Guenbour, E.M. Essassi, H. Oudda, Synergistic effect of potassium iodide with (E)-3-(4 methoxystyryl) quinoxalin-2 (1H)-one on the corrosio n inhibition of carbon steel in 1.0 M HCl, Der Pharma Chemica 7 (2015) 36-45, http://derpharmachemica.com/archive.html.

Laabaissi, T., Benhiba, F., Missioui, M., Rouifi, Z., Rbaa, M., Oudda, H., Ramli, Y., Guenbour, A., Warad, I., Zarrouk, A., 2020. Coupling of chemical, electrochemical and theoretical approach to study the corrosion inhibition of mild steel by new quinoxaline compounds in 1 M HCl. Heliyon 6,. https://doi.org/10.1016/j.heliyon.2020.e03939 e03939.

Badran, M.M., Abouzid, K.A.M., Hussein, M.H.M., 2003. Arch Pharm *Res* 26 (2), 107–113. https://doi.org/10.1007/BF02976653.

Singh, D.P., Deivedi, S.K., Hashim, S.R., Singhal, R.G., 2010. Pharmaceuticals 3 (8), 2416–2425. https://doi.org/10.3390/Ph3082416.

Wagle, S., Adhikari, A.V., Kumari, N.S., 2008. Ind J Chem 47 (3), 439–448.

Hui, X., Desrivot, J., Bories, C., Loiseau, P.M., Franck, X., Hocquemiller, R., Figadere, B., 2006. Bioorg. Med. Chem. Lett. 16 (4), 815–820. https://doi.org/10.1016/j.bmcl.2005.11.025.

Griffith, R.K., Chittur, S.V., Chen, Y.C., 1992. Med. Chem. Res. 2, 467–473.

El-Sabbagh, O.I., El-Sadek, M.E., Lashine, S.M., Yassin, S.H., El-Nabtity, S.M., 2009. Med. Chem. Res. 18 (9), 782–797. https://doi.org/10.1007/s00044-009-9203-y.

M. Loriga, S. Piras, P. Sanna, Paglietti (1997) Farmaco 52(3):157–166.

Balzarini, J., De Clercq, E., Carbonez, A., Burt, V., Kleim, J.-P., 2000. AIDS Res. Hum. Retroviruses 16 (6), 517–528.

Carta, A., Loriga, M., Priras, S., Paglietti, G., La Colla, P., Busonera, B., Collu, G., Loddo, R., 2006. Med. Chem. 2, 113–122. https://doi.org/10.2174/157340606776056197.

Ancizu, S., Moreno, E., Solano, B., Villar, R., Burguete, A., Torres, E., Pérez-Silanes, S., Aldana, I., Monge, A., 2010. New 3-methylquinoxaline-2-carboxamide 1,4-di-n-oxide derivatives as anti- mycobacterium tuberculosis agents. Bioorg Med Chem 18, 2713–2719. https://doi.org/10.1016/j.bmc.2010.02.024.

Carta, A., Sanna, P., Gherardini, L., Usai, D., Zanetti, S., 2001. Farmaco 56 (12), 933–938. https://doi.org/10.1016/S0014-827X(01)01161-2.

Guillon, J., Grellier, P., Labaied, M., Sonnet, P., Leger, J.M., Deprez-Poulain, R., Forfar-Bares, I., Dallemagne, P., Lemaître, N., Pehourcq, F., Rochette, J., Sergheraert, C., Jarry, C., 2004. J Med Chem 47, 1997–2009. https://doi.org/10.1021/jm0310840.

Gupta, D., Ghosh, N.N., Chandra, R., 2005. Synthesis and pharmacological evaluation of substituted 5-[4-[2-(6,7-dimethyl-1,2,3,4-tetrahydro-2-oxo-4-quinoxalinyl)ethoxy]phenyl]methylene]thiazolidine-2,4-dione derivatives as potent euglycemic and hypolipidemic agents. Bioorg. Med. Chem. Lett. 15, 1019–1022. https://doi.org/10.1016/j.bmcl.2004.12.041.

Lgaz, H., Salghi, R., Jodeh, S., Ramli, Y., Larouj, M., Toumiat, K., Quraishi, M.A., Oudda, H., Jodeh, W., 2016. Understanding the Adsorption of Quinoxaline Derivatives as Corrosion Inhibitors for Mild Steel in Acidic Medium: Experimental, Theoretical and Molecular Dynamic Simulation Studies. J. Steel. Struct. Constr. 2, 1000111J. https://doi.org/10.4172/2472-0437.1000111.

Zarrok, H., Zarrouk, A., Salghi, R., Ramli, Y., Hammouti, B., Al-Deyab, S.S., Essassi, E.M., Oudda, H., 2012. Int. J. Electrochem. Sci. 7, 8958–8973.

El Ouali, I., Hammouti, B., Aouniti, A., Ramli, Y., Azougagh, M., Essassi, E.M., Bouachrine, M., 2010. J. Mater. Envir. Sci. 1, 1–8.

Abboud, Y., Abourriche, A., Saffaj, T., Berrada, M., Charrouf, M., Bennamara, A., Himidi, N.A., Hannache, H., 2007. 2,3-Quinoxalinedione as a novel corrosion inhibitor for mild steel in 1 M HCl. Mater. Chem. Phys. 105, 1–5. https://doi.org/10.1016/j.matchemphys.2007.03.037.

Zarrok, H., Zarrouk, A., Salghi, R., Oudda, H., Hammouti, B., Ebn Touhami, M., Bouachrine, M., Pucci, O.H., Portugaliae, 2012. Electrochim. Acta 30, 405–417.

Tazouti, A., Galai, M., Touir, R., Ebn Touhami, M., Zarrouk, A., Ramli, Y., Saraçoğlu, M., Kaya, S., Kandemirli, F., Kaya, C., 2016. J. Mol. Liq. 221, 815–832.

el Aoufir, Y., Lgaz, H., Bourazmi, H., Kerroum, Y., Ramli, Y., Guenbour, A., Salghi, R., El-Hajjaji, F., Hammouti, B., Oudda, H., 2016. J. Mater. Environ. Sci. 7, 4330–4347.

Abdel-Megeed, M.A., Abdel-Rahman, H.M., Alkaramany, G.-E.-S., El-Gendy, M.A., 2009. Eur. J. Med. Chem. 44, 117. https://doi.org/10.1016/j.ejmech.2008.03.017.

Nowaczyk, A., Modzelewska-Banachiewicz, B., 2008. Triazole derivatives with antifungal activity: a pharmacophore model study. Acta Poloniae Pharmaceutica n Drug Research 65, 795.

Foroumadi, A., Mansouri, S., Kiani, Z., Rahmani, A., 2003. Synthesis and in vitro antibacterial evaluation of *N*-[5-(5-nitro-2-thienyl)-1,3,4-thiadiazole-2-yl] piperazinyl quinolones. Eur. J. Med. Chem. 38, 851. https://doi.org/10.1016/s0223-5234(03)00148-x.

Sato, Y., Shimoji, Y., Fujita, H., Nishino, H., Mizuno, H., Kobayashi, S., Kumakura, S., 2009. J. Med. Chem. 23 (8), 927.

Missioui, M., Said, M.A., Demirtas, G., Mague, J.T., Ramli, Y., 2022. Docking of Disordered Independent Molecules of Novel Crystal Structure of (N-(4-methoxyphenyl)-2-(3-methyl-2-oxo-3,4-dihydroquinoxalin-1(2H)-yl)acetamide as anti-Covid-19 and anti-Alzheimer's disease. Crystal structure, HSA/DFT/XRD, Journal of Molecular Structure 1247,. https://doi.org/10.1016/j.molstruc.2021.131420 131420.

Zhang, H., Zhang, J., Qu, W., Xie, S., Huang, L., Chen, D., Tao, Y., Liu, Z., Pan, Y., Yuan, Z., 2020. Design, synthesis, and biological evaluation of novel thiazolidinone– containing quinoxaline-1,4-di-N-oxides as antimycobacterial and antifungal agents. Front. Chem. 8, 598. https://doi.org/10.3389/fchem.2020.00598.

Shivarama Holla, B., Veerendra, B., Shivananda, M.K., 2003. Boja Poojary, Synthesis characterization and anticancer activity studies on some Mannich bases derived from 1,2,4-triazoles. Eur. J. Med. Chem. 38, 759. https://doi.org/10.1016/s0223-5234(03)00128-4.

Tron, G.C., Pirali, T., Billington, R.A., Canonico, P.L., Sorba, G., Genazzani, A.A., 2008. Click chemistry reactions in medicinal chemistry: applications of the 1,3-dipolar cycloaddition between azides and alkynes. Med. Res. Rev. 28, 278e308. https://doi.org/10.1002/med.20107.

Ferreira, S.B., Sodero, A.C.R., Cardoso, M.F.C., Lima, E.S., Kaiser, C.R., Silva, F.P., Ferreira, V.F., 2010. Synthesis, biological activity, and molecular modeling studies of 1H–1,2,3-triazole derivatives of carbohydrates as a-glucosidases inhibitors. J. Med. Chem. 53, 2364e2375. https://doi.org/10.1021/jm901265h.

Lauria, A., Delisi, R., Mingoia, F., Terenzi, A., Martorana, A., Barone, G., Almerico, A.M., 2014. 1,2,3-Triazole in heterocyclic compounds, endowed with biological activity, through 1,3-dipolar cycloadditions. Eur. J. Org. Chem. 16, 3289e3306. https://doi.org/10.1002/ejoc.201301695.

M. Nazir, M. A. Abbasi, Aziz-ur-Rehman , S. Z. Siddiqui , K. M. Khan, U. Salar , M. Shahid , M. Ashraf , M. A. Lodhi , F. A. Khan, Bioorganic Chemistry 81(2018) 253-263. 10.1016/j.bioorg.2018.08.010.

Gu, X., Yang, Y., Wang, Z., 2020. S. Afr. J. Bot. 133, 151–160. https://doi.org/10.1016/j.sajb.2020.07.021.

M. Alomari, M. Taha, F.Rahim, M. Selvaraj, N. Iqbal, S. Chigurupati , S. Hussain, N. Uddin, N. B. Almandil, M. Nawaz, R. K. Farooq, K. M. Khan, Synthesis of indole-based-thiadiazole derivatives as a potent inhibitor of α-glucosidase enzyme along with in silico study, Bioorgan. Chem. 108(2021)104638. 10.1016/j.bioorg.2021.104638.

Hussain, S., Taha, M., Rahim, F., Hayat, S., Zaman, K., Iqbal, N., Selvaraj, M., Sajid, M., Bangesh, M.A., Khan, F., Khan, K.M., Uddin, N., Shah, S.A.A., Ali, M., 2021. J. Mol. Struct. https://doi.org/10.1016/j.molstruc.2021.130029.

Tavaf, Z., Dangolanib, S.K., Yousefi, R., Panahib, F., Shahsavani, M.B., Khalafi-Nezhad, A., 2020. Carbohydr. Res. 494,. https://doi.org/10.1016/j.carres.2020.108069 108069.

Missioui, M., Mortada, S., Guerrab, W., Serdaroğlu, G., Kaya, S., Mague, J.T., Essassi, E.M., Faouzi, M.E.A., Ramli, Y., 2021. Novel antioxidant quinoxaline derivative: Synthesis, crystal structure, theoretical studies, antidiabetic activity and molecular docking study. J. Mol. Struct. 1239,. https://doi.org/10.1016/j.molstruc.2021.130484 130484.

Wang, G., Li, X., Wang, J., Xie, Z., Li, L., Chen, M., Chen, S., Peng, Y., 2017. Synthesis, molecular docking and a-glucosidase inhibition of 2-((5,6-diphenyl-1,2,4-triazin-3-yl) thio)-N-arylacetamides. Bioorg. Med. Chem. Lett. 27, 1115–1118. https://doi.org/10.1016/j.bmcl.2017.01.094.

Moghimi, S., Toolabi, M., Salarinejad, S., Firoozpour, L., Esmaeil, S., Ebrahimi, S., Safari, F., Mojtabavi, S., Faramarzi, M.A., Forouma, A., 2020. Bioorg. Chem. 102,. https://doi.org/10.1016/j.bioorg.2020.104071 104071.

R. M. Asath, T.N. Rekha, S. Premkumar, T. Mathavan, A. Milton Franklin Beni, Journal of Molecular Structure 1125(2016) 633–642. 10.1016/j.molstruc.2016.07.064.

G-J. Ye, T. Lan, Z-X. Huang, X-N Cheng, C-Y. Cai, S-M. Ding, M-L. Xie, B. Wang, Eur. J. Med. Chem. 177 (2019) 362e373, 10.1016/j.ejmech.2019.05.045.

Zaoui, Y., Ramli, Y., Tan, S.L., Tiekink, E.R.T., Chemlal, L., Mague, J.T., Taoufik, J., Faouzi, M.E.A., Ansar, M.H., 2021. Synthesis, structural characterisation and theoretical studies of a novel pyridazine derivative: Investigations of anti-inflammatory activity and inhibition of α-glucosidase. J. Mol. Struct. 1234,. https://doi.org/10.1016/j.molstruc.2021.130177 130177.

Abad, N., Sallam, H.H., Al-Ostoot, F.H., Khamees, H.A., Al-horaibi, S.A., Khanum, S.A., Madegowda, M., El Hafi, M., Mague, J.T., Essassi, E.M., Y., 2021. Ramli Synthesis, crystal structure, DFT calculations, Hirshfeld surface analysis, energy frameworks, molecular dynamics and docking studies of novel isoxazolequinoxaline derivative (IZQ) as anti-cancer drug. J. Mol. Struct. 1232,. https://doi.org/10.1016/j.molstruc.2021.130004 130004.

Abad, N., Ferfra, S., Essassi, E.M., Mague, J.T., Ramli, Y., 2021. Synthesis and crystal structure of 1-octyl-3-phenylquinoxalin-2(1H)-one, $C_{22}H_{26}N_2O$. Zeitschrift für Kristallographie-New Crystal Structures 236, 173–175. https://doi.org/10.1515/ncrs-2020-0404.

Guerrab, W., Missioui, M., Zaoui, Y., Mague, J.T., Ramli, Y., 2021. Synthesis and crystal structure of 2-azido-N-phenylacetamide, C8H8N4O. Zeitschrift für Kristallographie-New Crystal Structures 236, 133–134. https://doi.org/10.1515/ncrs-2020-0409.

Guerrab, W., Lgaz, H., Kansiz, S., Mague, J.T., Dege, N., Ansar, M., Marzouki, R., Taoufik, J., Ali, I.H., Chung, I.M., Ramli, Y., 2019. Synthesis of a novel phenytoin derivative: crystal structure, Hirshfeld surface analysis and DFT calculations. J. Mol. Struct. 1205,. https://doi.org/10.1016/j.molstruc.2019.127630 127630.

W. Guerrab, M.Jemli, J. Akachar, G.Demirtaş , J.T. Mague, A. Ibrahimi, Jamal Taoufik, M. Ansar, K. Alaoui & Y. Ramli, Design, synthesis, structural and molecular characterization, toxicity, psychotropic activity and molecular docking evaluation of a novel phenytoin derivative: 3-decyl-5,5-diphenylimidazolidine-2,4-dione, Journal of Biomolecular Structure and Dynamics, In press, 10.1080/07391102.2021.1922096.

Hinsberg, O., 1887. Liebigs Ann. Chem. 237, 1228.

Benzeid, H., Ramli, Y., Vendier, L., Essassi, E.M., Ng, S.W., 2009. 3-Methyl-1-propargylquinoxalin-2(1H)-one. Acta Cryst. E65, o2196.

Bruker *APEX3*, *SAINT*, *SADABS* & *SHELXTL*, Bruker AXS, Inc., Madison, WI. (2016).
Sheldrick, G.M., 2015. Acta Cryst. A 71, 3–8. https://doi.org/10.1107/S2053273314026370.
Sheldrick, G.M., 2015. Acta Cryst. C 71, 3–8. https://doi.org/10.1107/S2053229614024218.
Brandenburg, K., Putz, H., 2012. DIAMOND. Crystal Impact GbR, Bonn, Germany.
G. M. Sheldrick, Univ. of Göttingen, Göttingen, Germany (2008).
Bruker-AXS, LLC, Madison, WI, USA (2019).
Sheldrick, G.M., 2009. TWINABS. University of Göttingen, Göttingen, Germany.
Kee, K.T., Koh, M., Oong, L.X., Ng, K., 2013. Screening culinary herbs for antioxidant and α-glucosidase inhibitory activities. Int J Food Sci Technol 48, 1884–1891. https://doi.org/10.1111/ijfs.12166.
Mortada, S., Missioui, M., Guerrab, W., Demirtaş, G., Mague, J.T., Faouzi, M.E.A., Ramli, Y., 2022. New styrylquinoxaline: synthesis, structural, biological evaluation, ADMET prediction and molecular docking investigations. J. Biomol. Struct. Dyn. https://doi.org/10.1080/07391102.2022.2040592.
Hashim, A., Khan, M.S., Khan, M., Sajid, B., Mohd, H., Ahmad, S., 2013. Antioxidant and α -Amylase Inhibitory Property of *Phyllanthus virgatus* L.: An *In Vitro* and Molecular Interaction Study. Biomed Res. Int. 2013, 1–12. https://doi.org/10.1155/2013/729393.
Tuberoso, C.I.G., Boban, M., Bifulco, E., Budimir, D., Pirisi, F.M., 2013. Antioxidant capacity and vasodilatory properties of Mediterranean food: The case of Cannonau wine, myrtle berries liqueur and strawberry-tree honey. Food Chem. 140, 686–691. https://doi.org/10.1016/j.foodchem.2012.09.071.
J.R.C. M.J. Frisch, G.W. Trucks, H.B. Schlegel, G.E. Scuseria, M.A. Robb, S.S.I. J.A. Montgomery, Jr., T. Vreven, K.N. Kudin, J.C. Burant, J.M. Millam, G.A.P. J. Tomasi, V. Barone, B. Mennucci, M. Cossi, G. Scalmani, N. Rega, T. H. Nakatsuji, M. Hada, M. Ehara, K. Toyota, R. Fukuda, J. Hasegawa, M. Ishida, H.P.H. Nakajima, Y. Honda, O. Kitao, H. Nakai, M. Klene, X. Li, J.E. Knox, A.J. J.B. Cross, C. Adamo, J. Jaramillo, R. Gomperts, R.E. Stratmann, O. Yazyev, G.A. Austin, R. Cammi, C. Pomelli, J.W. Ochterski, P.Y. Ayala, K. Morokuma, A.D.D. Voth, P. Salvador, J.J. Dannenberg, V.G. Zakrzewski, S. Dapprich, J.B.F. M.C. Strain, O. Farkas, A.D. Rabuck, D.K. Malick, K. Raghavachari, A. J.V. Ortiz, Q. Cui, A.G. Baboul, S. Clifford, J. Cioslowski, B.B. Stefanov, G. Liu, M.A.A.-L. Liashenko, P. Piskorz, I. Komaromi, D.J. Fox, R.L. Martin, T. Keith, W.C. C.Y. Peng, A. Nanayakkara, B. Johnson, M. Challacombe, P.M.W. Gill, J.A.P. M.W. Wong, C. Gonzalez, Gaussian 03, Revision C.02, Gaussian, Inc., Wallingford CT, (2004).
Becke, A.D., 1993. Density-functional thermochemistry. III. The role of exact exchange. J. Chem. Phys. 98, 5648–5652. https://doi.org/10.1063/1.464913.
Lee, C., Yang, W., Parr, R.G., 1988. Development of the Colle-Salvetti correlation-energy formula into a functional of the electron density. Phys. Rev. B. 37, 785–789. https://doi.org/10.1103/PhysRevB.37.785.
Miehlich, B., Savin, A., Stoll, H., Preuss, H., 1989. Results obtained with the correlation energy density functionals of becke and Lee, Yang and Parr. Chem. Phys. Lett. 157, 200–206. https://doi.org/10.1016/0009-2614(89)87234-3.
J.A. Pople, P. V. Schleyer, W.J. Hehre, L. Radom, AB INITIO molecular orbital theory, 1986. 10.1016/s0022-328x(00)99651-7.
Æ. Frisch, R.D. Dennington II, T.A. Keith, J. Millam, A.B. Nielsen, A.J. Holder, J. Hiscocks, GaussView 4, (2007). www.gaussian.com.
Spackman, M.A., Byrom, P.G., 1997. A novel definition of a molecule in a crystal. Chem. Phys. Lett. 267, 215–220. https://doi.org/10.1016/S0009-2614(97)00100-0.
McKinnon, J., Mitchell, A.S., Spackman, M.A., 1998. Visualising intermolecular interactions in crystals: naphthalene vs. terephthalic acid. Chem. Commun., 2071–2072 https://doi.org/10.1039/a804691c.
Spackman, M.A., McKinnon, J.J., 2002. Fingerprinting intermolecular interactions in molecular crystals. CrystEngComm 4, 378–392. https://doi.org/10.1039/B203191B.
D. S. K. Wolff, D. J. Grimwood, J. J. McKinnon, M. J. Turner, J. and M.A. Spackman, CrystalExplorer (Version 3.1), Univ. West. Aust. (2012). 10.1039/b704980c.
Williams, L.K. et al, 2012. Order and disorder: differential structural impacts of myricetin and ethyl caffeate on human amylase, an antidiabetic target. J. Med. Chem. ACS Publications 55, 10177–10186.
V. Roig-Zamboni, *et al.* 'Structure of human lysosomal acid α-glucosidase–a guide for the treatment of Pompe disease', Nature communications. Nature Publishing Group, 8(1), pp. 1–10.
Trott, O., Olson, A.J., 2010. AutoDock Vina: improving the speed and accuracy of docking with a new scoring function, efficient optimization, and multithreading. J. Comput. Chem. 31 (2017), 455–461. https://doi.org/10.1002/jcc.21334.
Hermans, M.M. et al, 1991. Human lysosomal alpha-glucosidase Characterization of the catalytic site'. J. Biol. Chem. 266 (21), 13507. https://doi.org/10.1016/S0021-9258(18)92727-4.
Roig-Zamboni, V. et al, 2017. Structure of human lysosomal acid α-glucosidase–a guide for the treatment of Pompe disease. Nature communications. Nature Publishing Group 8 (1), 1–10. https://doi.org/10.1038/s41467-017-01263-3.
Y. Ramli, H. Benzeid, R. Bouhfid, Y. Kandri Rodi, S. Ferfra, E.M. Essassi, Synthesis, reactivity and biological activity of quinoxalin-2-one derivatives, Studiişi Cercetări Ştiinţifice Chimieşi Inginerie Chimică, Biotehnologii, Industrie Alimentară 11 (2010) 67-90, CSCC6201011V01S01A0005 [0002970].
Liu, Y., Ma, L., Chen, W., Wang, B., Xu, Z.L., 2007. Synthesis of xanthone derivatives with extended p systems as a-glucosidase inhibitors: insight into the probable binding mode. Bioorg. Med. Chem. 15, 2810e2814. https://doi.org/10.1016/j.bmc.2007.02.030.
Li, G.L., He, J.Y., Zhang, A., Wan, Y., Wang, B., Chen, W.H., 2011. Toward potent aglucosidase inhibitors based on xanthones: a closer look into the structureactivity correlations. Eur. J. Med. Chem. 46, 4050e4055. https://doi.org/10.1016/j.ejmech.2011.06.003.
Wang, G., Peng, Z., Wang, J., Li, J., Li, X., 2016. Synthesis and biological evaluation of novel 2,4,5-triarylimidazole-1,2,3-triazole derivatives via click chemistry as α-glucosidase inhibitors. Bioorg. Med. Chem. Lett 26, 5719e5723. https://doi.org/10.1016/j.bmcl.2016.10.057.
Wang, G., Peng, Z., Wang, J., Li, X., Li, J., 2017. Synthesis, in vitro evaluation and molecular docking studies of novel triazine-triazole derivatives as potential α-glucosidase inhibitors. Eur. J. Med. Chem. 125, 423e429. https://doi.org/10.1016/j.ejmech.2016.09.067.
Abad, N., Hajji, M., Ramli, Y., Belkhiria, M., Elmgirhi, S.M.H., Habib, M.A., Guerfel, T., Mague, J.T., Essassi, E.M., 2020. A newly synthesized nitrogen-rich derivative of bicyclic quinoxaline—Structural and conceptual DFT reactivity study. J. Phys. Org. Chem. 33,. https://doi.org/10.1002/poc.4055 e4055.
Missioui, M., Lgaz, H., Guerrab, W., Lee, H., Warad, I., Mague, J. T., Ali, I.H., Essassi, E.M., Ramli, Y., 2022. Synthesis of novel hybrid quinoxaline containing triazole and acetamide moieties by azide-alkyne click chemistry: Experimental and theoretical characterization. J. Mol. Struct. 1253,. https://doi.org/10.1016/j.molstruc.2021.132132 132132.
Hathwar, V.R., Sist, M., Jørgensen, M.R.V., Mamakhel, A.H., Wang, X., Hoffmann, C.M., Sugimoto, K., Overgaard, J., Iversen, B.B., 2015. Quantitative analysis of intermolecular interactions in orthorhombic rubrene. IUCrJ. 2, 563–574. https://doi.org/10.1107/S2052252515012130.
Okulik, N., Jubert, H., 2005. Theoretical Analysis of the Reactive Sites of Non–steroidal Anti–inflammatory Drugs. Internet Electron. J. Mol. Des. 4, 17–30.

Luque, F.J., López, J.M., Orozco, M., 2000. Perspective on "Electrostatic interactions of a solute with a continuum. A direct utilization of ab initio molecular potentials for the prevision of solvent effects". Theor. Chem. Accounts Theory, Comput. Model. (Theoretica Chim. Acta). 103, 343–345. https://doi.org/10.1007/s002149900013.

Scrocco, E., Tomasi, J., 1978. Electronic Molecular Structure, Reactivity and Intermolecular Forces: An Euristic Interpretation by Means of Electrostatic Molecular Potentials. in, 115–193. https://doi.org/10.1016/S0065-3276(08)60236-1.

Seth, S.K., Maity, G.C., Kar, T., 2011. Structural elucidation, Hirshfeld surface analysis and quantum mechanical study of para-nitro benzylidene methyl arjunolate. J. Mol. Struct. https://doi.org/10.1016/j.molstruc.2011.06.003.

Luo, Y.H., Sun, B.W., 2013. Pharmaceutical co-crystals of pyrazinecarboxamide (PZA) with various carboxylic acids: Crystallography, hirshfeld surfaces, and dissolution study. Cryst. Growth Des. https://doi.org/10.1021/cg400167w.

Fleming, I., Wiley, J., 1979. Frontier Orbitals and Organic Chemical Reactions. Front. Orbitals Org. Chem. React. https://doi.org/10.1016/0022-2860(79)80172-6.

Yousef, T.A., Alduaij, O.K., Ahmed, S.F., Abu El-Reash, G.M., El-Gammal, O.A., 2016. Structural, DFT and biological studies on Cr (III) complexes of semi and thiosemicarbazide ligands derived from diketo hydrazide. J. Mol. Struct. 1125, 788–799. https://doi.org/10.1016/j.molstruc.2016.07.045.

Agrawal, M., Deval, V., Gupta, A., Sangala, B.R., Prabhu, S.S., 2016. Evaluation of structure-reactivity descriptors and biological activity spectra of 4-(6-methoxy-2-naphthyl)-2-butanone using spectroscopic techniques. Spectrochim. Acta A 167, 142–156. https://doi.org/10.1016/j.saa.2016.04.053.

Wu, S., Qi, L., Ren, Y., Ma, H., 2020. 1,2,4-triazole-3-thione Schiff bases compounds: Crystal structure, hirshfeld surface analysis. DFT Stud. Biol. Eval. 1219,. https://doi.org/10.1016/j.molstruc.2020.128591 128591.

Pearson, R.G., 2005. Chemical hardness and density functional theory. J. Chem. Sci. 117, 369–377. https://doi.org/10.1007/BF02708340.

Koopmans, T., 1934. Über die Zuordnung von Wellenfunktionen und Eigenwerten zu den Einzelnen Elektronen Eines Atoms. Physica. 1, 104–113. https://doi.org/10.1016/S0031-8914(34)90011-2.

Parr, R.G., Pearson, R.G., 1983. Absolute hardness: companion parameter to absolute electronegativity. J. Am. Chem. Soc. 105, 7512–7516. https://doi.org/10.1021/ja00364a005.

A. Kerflani, K. Si Larbi, A. Rabahi, A. Bouchoucha, S. Zaater, and S. Terrachet-Bouaziz, 'Novel palladium (II) complexes with iminocoumarin ligands: Synthesis, characterisation, electrochemical behaviour, DFT calculations and biological activities, ADMET study and molecular docking', Inorganica Chimica Acta, vol. 529, p. 120659, Jan. 2022, 10.1016/j.ica.2021.120659.

Lipinski, C.A., Lombardo, F., Dominy, B.W., Feeney, P.J., 2001. Experimental and computational approaches to estimate solubility and permeability in drug discovery and development settings. Adv Drug Deliv Rev 46 (1–3), 3–26. https://doi.org/10.1016/s0169-409x(00)00129-0.

'SwissADME'. http://www.swissadme.ch/ (accessed Dec. 15, 2021).

'ADMETlab 2.0'. https://admetmesh.scbdd.com/ (accessed Sep. 24, 2021).

Adedotun, I.O. et al, 2022. Molecular docking, ADMET analysis, and bioactivity studies of phytochemicals from Phyllanthus niruri as potential inhibitors of hepatitis C virus NSB5 polymerase. J. Indian Chem. Soc. 99, (2). https://doi.org/10.1016/j.jics.2021.100321 100321.

Ferreira, L.L.G., Andricopulo, A.D., 2019. ADMET modeling approaches in drug discovery. Drug Discovery Today 24 (5), 1157–1165. https://doi.org/10.1016/j.drudis.2019.03.015.